Bimodal seismic-aseismic behavior of a weakly coupled megathrust segment revealed by kinematic analysis of a seismic swarm and slow slip event offshore Copiapó, Chile

This manuscript has been submitted for publication in *Earth and Planetary Science Letters*. Please note that it has not yet been reviewed.

E. Klein[a,1], J. Ojeda[b], B. Rousset[c], C. Vigny[a], S. Ruiz[d], B. Potin[d], J.C. Baez[e], D. Zigone[c]

[a] *Laboratoire de géologie - CNRS UMR 8538, École normale supérieure - PSL University, Paris, France*
[b] *Departamento de Ingeniería Civil, Universidad de Concepción, Concepción, Chile*
[c] *Institut Terre et Environnement de Strasbourg, Université de Strasbourg, CNRS UMR 7063, Strasbourg, France*
[d] *Departamento de Geofísica, Universidad de Chile, Santiago, Chile*
[e] *Centro Sismológico Nacional, Universidad de Chile, Santiago, Chile*

Abstract

A seismic swarm occurred in Chile in 2023, in a region well known for hosting this type of seismicity, the Atacama region, and more precisely within the low coupling zone of Barranquilla. It started on August 26th and lasts about 6 weeks, ending early October. Thanks to our high-density small-scale GNSS network, we recorded the spatio-temporal evolution of surface deformation generated by a slow slip event associated with the swarm. The slow slip event lasts as long as the seismic swarm but takes place in two distinct phases, located on two distinct patches of slip. Overall, the cumulative slip distribution extends over about 100 km (between 27° S and 28° S), reaching an equivalent Mw 6.1. The two patches of slip exhibit a quite different in-

*Correspondence to: klein@geologie.ens.fr

terplay between aseismic slip and seismicity, revealing bimodal seismic and aseismic behaviors. In the northern patch, which hosted almost all known swarms and where higher coupling was found, slip is collocated with seismicity, exhibiting important brittle deformation. In contrast, in the southern patch where coupling is low, microseismicity is not collocated with slip and is most likely driven by Coulomb stress transfer, suggesting a dominant aseismic behavior. We therefore demonstrate that the SSE associated with the 2023 swarm reveals the details of the low coupling zone structure that slow, interseismic deformation could not entirely decipher. Investigations on the long-term seismicity suggest that the aseismic behavior of the low coupling zone southern part has persisted at least since seismicity was cataloged and plausibly at the timescale of the regional seismic cycle.

Keywords:

---

*[1]

1. Introduction

Our understanding of the processes involved in the seismic cycle, and in particular the interseismic phase, has evolved rapidly and dramatically thanks to the exponential increase in GNSS observation networks across all fault zones worldwide, particularly subduction zones. Thanks to the precise measurement of surface deformation during the interseismic period, numerous coupling models at the interface between the two plates have been proposed for almost all subductions (Oryan et al., 2026). The lateral segmentation highlighted by coupling models (e.g., Cascadia Bruhat and Segall (2016), Japan Loveless and Meade (2010), South America Nocquet et al. (2014); Métois et al. (2016)), combined with historical seismicity, has thus enabled the identification of seismic gaps. In the case of the most recent earthquakes, there is a good correspondence between the previously strongly coupled surfaces and the seismic rupture surfaces (Ruegg et al., 2009; Madariaga et al., 2010; Métois et al., 2016; Loveless and Meade, 2011). Pre-seismic coupling could therefore be a good predictor of future seismic rupture. However, this idea faces a major obstacle.

Even though the different coupling models published for a given area appear consistent at first glance, they differ significantly in their details. These differences stem mainly from either the input data (measured inter-seismic

velocities) or the assumptions underlying the inversions (smoothing, damping, boundary conditions, etc.). Consequently, the quantitative correlation between a given coseismic slip model and any pre-seismic coupling pattern is highly variable, and sometimes poor. In particular, even if the surface rupture and the highly coupled surface correspond well, the precise amount of coseismic slip seems rather uncorrelated to the prior coupling amplitudes. What information can be considered robust and interpretable in terms of seismic hazard? In particular, the precise quantification of Low Coupled Zones (LCZs), the weakly coupled zones separating large asperities that accumulate deformation, is critical but necessary in order to discuss their ability to act as a barrier to seismic rupture. However, the surface area and amount of decoupling in LCZs can vary significantly from one model to another. Interseismic data are clearly insufficient to characterize them accurately, probably because the small deformation rate (2 cm/yr, i.e., 0.05 mm/day) leaves too much room for variability among models. More robust information is needed on the surface area and amount of decoupling in LCZs.

GNSS has also revealed slow slip events (SSEs) and other episodic tremor and slip events (ETSs), which are now known to occur in most subduction zones (Wallace and Rollins, 2024), even if occasionally unadapted networks do not necessarily allow them to be observed clearly. Shallow SSEs appear to occur in LCZs, or at least in zones transitioning from strong to low coupling and often are accompanied by seismic swarms (e.g., Uchida et al., 2016; Vaca et al., 2018; Rolandone et al., 2018; Dixon et al., 2014). Some SSEs have been found to be precursors to major earthquakes, e.g., in Mexico (Radiguet et al., 2016; Graham et al., 2014), Japan (Ozawa et al., 2025), Nicaragua (Voss et al., 2018), and also in Chile, in Iquique 2014 (Socquet et al., 2017; Boudin et al., 2022), or in Valparaiso 2017 (Ruiz et al., 2017; Caballero et al., 2021; Moutote et al., 2023; Ruiz et al., 2025). While we do not yet know what causes an SSE to be a precursor to an earthquake, their study remains of paramount importance. SSEs produce larger deformation rates ($\sim$0.1 mm/day) than assumed linear interseismic deformation ($\sim$ 0.05 mm/day). Thus, detailed SSEs analysis can depict the finer spatio-temporal evolution of plate coupling that is invisible under the linear interseismic assumption. Subduction segments where dense geodetic networks capture both interseismic deformation and recurrent transient slip offer a unique opportunity to address this problem. North Central Chile is one of these natural laboratories, thanks to the decades-long geodetic monitoring of this area (Métois et al., 2014; Klein et al., 2018b, 2021).

This article focuses on the SSE associated with the seismic swarm that occurred there in 2023. This region constitutes one of the major seismic gaps in the Chilean subduction zone and appears mature for a future large rupture (Kelleher, 1972; Beck et al., 1998; Carvajal et al., 2017; Ruiz and Madariaga, 2018). The long-term coupling pattern closely matches the revisited historical seismicity, with the Atacama segment to the south corresponding to the 1922 M∼8.5 rupture and the Chañaral segment to the north corresponding to the 1918 M∼8 rupture (Vigny et al., 2024). Furthermore, geoarchaeological evidence suggests that the giant earthquake that ruptured much of northern Chile ∼3,800 years ago also affected this region (Salazar et al., 2022). In addition to its high seismic hazard, this region appears to be one of the few places along the Chilean margin where a broad spectrum of slip behaviors can be simultaneously observed, possibly because it is currently among the most instrumented regions of the Chilean subduction zone (Klein et al., 2021; Zigone et al., 2019; Socquet et al., 2020).

The most recent event is a seismic swarm that occurred between August and October 2023, in a specific area of North Central Chile, well known for hosting this kind of activity (∼ 27.8° S). In contrast to the 2006 swarm, which was marked by two Mw∼6.5 earthquakes (Ojeda et al., 2023), the largest events in 2023 reached only Mw∼5.7 (15/09/2023, Centro Sismológico Nacional, CSN) and Ml∼5.3 (Münchmeyer et al., 2025c, 11/09/2023). Previous work inferred a ∼1-month-long, of about 100 km long transient deformation from 18 continuous GNSS stations and proposed that fluid overpressure around subducted seamounts controls both swarm activity and slow slip initiation (Münchmeyer et al., 2025c).

Here, we report a more detailed view of the 2023 swarm and associated SSE based on a dense near-field GNSS network, allowing for high spatial and temporal resolution. Despite the small amplitude of the deformation, the data accurately resolve the kinematics of the SSE. We image a two-phase event, propagating from north to south, consistent with the seismicity, within the LCZ of Barranquilla. The seismic-aseismic interplay differs between the two main slipping areas, revealing two distinct frictional behaviors. This event therefore provides a high-resolution image of the internal structure of the LCZ and new constraints on the physics of megathrust slip.

2. Seismotectonic context of the region of Atacama

The Atacama region in North Central Chile ($\sim$ 26 - 29° S) is particularly complex due to numerous events of different types, including a diversity of slip modes, that occurred there during the last two decades of continuous geodetic and seismological monitoring.

Different coupling models have been proposed in this region since the beginning of dense measurements there in 2010 (Métois et al., 2014; Métois et al., 2016; Klein et al., 2018b; González-Vidal et al., 2023; Yáñez-Cuadra et al., 2022). At the first order, the segmentation of the North Central Chilean region appears quite consistent in all models, with two highly coupled patches, Atacama to the South and Chañaral to the North, separated by the LCZ of Barranquilla at $\sim$ 27.7° S. At second order, the description of the LCZ differs significantly in terms of extension and location, as well as in the amplitude of decoupling.

In this region, seismic swarms have been observed since the 70's, and GNSS measurements, initiated in the 2000's, have uncovered different transient events. They can be categorized into three slip modes, based on their seismo-tectonic characteristics and location. We detail here the characteristics of these slip modes and the timeline of known events shown in Fig. 1-B.

The Sequence of Atacama. In 2020, a complex seismic/aseismic sequence, characterized by three earthquakes of Mw greater than 6 occurring on the same day, took place around 28° S (in orange on Fig. 1, Klein et al. (2021)). The last two earthquakes were most likely triggered by rapid post-seismic slip induced by the first earthquake, accompanied by migrating microseismicity. This sequence was also marked by a significant post-seismic deformation spreading northward, within the least coupled part of the Barranquilla LCZ (in yellow on Fig. 1). A potential similar sequence may have happened in December 2011 (Ojeda et al., 2023), and the same area was identified as a seismicity cluster by (Potin et al., 2025).

Recurrent Deep Slow Slip Event of Copiapó. Further north ($\sim$ 27.2° S), between 40 and 60 km depth, down-dip of the seismogenic zone beneath the city of Copiapó, a SSE occurs every 5 years or so (in pink on Fig. 1). The last occurrence, in 2020, was precisely captured and quantified by cGNSS and later by InSAR measurements (Klein et al., 2023; Molina-Ormazabal et al., 2025). The precedent occurrence in 2014 had been observed by survey

GNSS, while that in 2009 was visible in the single cGNSS station operating at the time (Klein et al., 2018a). To this day, no evidence of associated tectonic tremors, low-frequency earthquakes, or other unusual seismicity has been found (Münchmeyer et al., 2025a).

Seismic swarms offshore Copiapó. At the same latitude as the deep SSE but offshore, seismic swarms have occurred on many occasions, with certainty in 1973, 1979, 2006, and 2015 (Holtkamp et al., 2011; Marsan et al., 2023). The 2015 swarm was relatively small and produced no observable deformation by the then sparse GNSS network. The 2006 swarm, by contrast, was quite large, and possible evidence of aseismic slip was detected for the first time. But GNSS networks were then too scarce to discriminate the large postseismic deformation triggered by the two Mw 6.5 earthquakes from any other SSE (Ojeda et al., 2023). The 2023 swarm, which is the object of our study, is therefore the very first occasion to investigate precisely the processes at stake during this type of event. Given their proximity and the fact that they occurred offshore, we'll refer to them as the Caldera seismic swarms.

To date, no direct relation has been established between deep SSEs beneath Copiapó and the shallow seismic swarms offshore Caldera. Nevertheless, the subduction of the Copiapó Ridge at this latitude, which is characterized by a series of heterogeneous seamounts (Fig. 1), may have important implications on the diversity of slip modes at the plate interface and surroundings, defining along-dip and along-strike segmentation (Pastén-Araya et al., 2022).

3. Data & Methods

3.1. GNSS Data processing and post-processing

We use the up-to-date GNSS daily position time series database *SOAM_GNSS_solENS*, distributed through the Geodesy Plotter (Klein, 2025). The solution is standard state-of-the-art GAMIT/GLOBK double-differences processing (IGS precise orbits, ionospheric free combination and ambiguity resolution) and aligned with ITRF2014 using the PYACS toolbox (Herring et al., 2010a,b; Nocquet and Tran, 2025). For more details about the processing, refer to Klein et al. (2022). We select stations in Chile located between 24° and 31° S from the CSN and COP2020 networks (Báez et al., 2018; Klein et al., 2021).

In this work, we focus on the period between 2019 and 2024. Time series are detrended using a local trend estimated over the period 2021 - 2023.5. This trend differs from the interseismic steady-state velocity because southern stations are affected by post-seismic deformation from both the 2015 Illapel earthquake and the 2020 sequence (Boulze et al., 2022; Klein et al., 2021). This method allows the transient signal associated with the 2023 Caldera swarm to be identified. A common mode filter (Fig. 2) is estimated and subtracted. Daily scatter is smoothed out by applying a 30-day sliding-window mean filter. The smoothed time series clearly shows a small but significant transient deformation on the horizontal component, spanning several weeks. No significant signal is visible on the vertical component (see Figs. S1 and S2). Then, weekly displacements are estimated between August and December.

Nothing looks more like SSE than common modes. It is common knowledge that GNSS position time series depict oscillations and transient signals. They can be either real, associated with seasonal deformation or with tectonic motions, or they can be more chaotic and associated with noise. Since a significant part of the noise can be associated with reference frame oscillations or any other large scale issue, the estimation of common mode is the best way to get rid of it. In the following section, we show how such transient signals, when not properly removed by a common mode can spread an instantaneous co-seismic jump over days and even weeks, making it look like aseismic transient deformation.

The preliminary observation of raw time series (before common mode and sliding window filters) of stations in the area of interest reveals two quite large and distinct ramps. The first one starts in early September, mostly visible north of 28.5° S (highlighted in yellow on Fig. 2). A second ramp starts mid-October (highlighted in green on Fig. 2). Both ramps depict very similar amplitudes (up to 5 mm on the East component), but the second one exhibits a quite shorter duration, which implies a faster motion. According to the CSN catalog, a Mw 6.6 earthquake occurred some 50 km from Vallenar (28° S), off the coast, on October 31st, ie a few weeks after the apparent onset of the transient phenomenon. But no coseismic offset is visible in the time series. A 3-weeks cumulative displacement field typical of a shallow source, ie westward convergent direction affecting a 100 km region between 28.5 and 29.5° S can be inferred from this signal. However, the common mode estimated over far-field station completely removes this signal. On the

opposite, the first ramp remains. (see VALL time series, Fig. 2-C and the 3 components time series on Figs. S1 and S2) To ensure this result, we test two types of common mode filter: The first filter (CMM1, Fig. 2-A) is estimated with time series from a selection of stations located sufficiently far from the region of interest (PEDR, PFRJ, PVCA, RODE, BTON, TOLO, MRCG, INCA, PAZU), in order to ensure that they are not affected by the SSE or the Mw6.6. Since the network is much denser in the south (region of Illapel), than in the north, more stations located in the south are selected, which may impact the common mode correction.
The second filter is estimated with time series of all stations in the region between 31° S and 26° S, therefore including areas affected by transient deformation. Since the SSE only impacts a specific area, its deformation is not considered a common mode. Only a common mode estimated with too few far field station stations may be corrupted by the near field transient.
Both filters are very similar (see Fig. S3) and lead to the same conclusion: the early-September ramp remains while the end-October ramp disappears, leaving only a small but clear co-seismic step on some time series. The first transient, which is therefore real, can be associated with the 2023 swarm. The second transient, which could have been associated with aseismic slip preceding the 31st October earthquake, is an artefact. Thus, caution is advised when analyzing and interpreting transient signals in GNSS time series.

3.2. Kinematic slip inversion methodology

Our analysis allows us to capture the spatio-temporal evolution of surface deformation during the 2023 swarm through weekly snapshots. We can either look at cumulative deformation (blue vectors, Fig. 1) or at weekly displacement rates (red vectors, Fig. 3). Using these deformation fields and constrained least squares inversions with the CSI toolbox, we evaluate the slip distribution and spatio-temporal evolution of the SSE (Gombert et al., 2019).
The fault plane geometry is taken from Münchmeyer et al. (2025b) and is composed of triangular sub-faults. Tests made with the Slab2.0 geometry (Hayes et al., 2018) provides very similar results. Green functions are calculated assuming a layered Earth model (Husen et al., 1999; Zhu and Rivera, 2002). We parametrize the geometry so that slip is the linear interpolation of inverted slip values at each nodes of the patches (Jolivet et al., 2020, 2023). One slip component is allowed, which direction is assumed to be the projection of the plate (convergence vector Klein et al., 2018b) onto the subduction

interface, forbidding back slip in the thrust direction. Weekly slip rates are then inverted, in a quasi-kinematic scheme without including any additional temporal smoothing. Indeed, we consider that the median filter over 30-days window applied on position time series already plays that role.

3.3. Coulomb failure stress change analysis

To characterize potential interactions between aseismic slip and seismicity rates within local seismic clusters, we computed the Coulomb failure stress change (ΔCFS) induced by weekly aseismic slip rates. ΔCFS was calculated on the same interface patches used for the slip inversion using the algorithm of Nikkhoo and Walter (2015). We used Lamé parameters μ and λ of 30 GPa and a friction coefficient of 0.4. ΔCFS was computed only outside the slipping area for different weekly slip-rate thresholds (from 4 to 7 mm/week). ΔCFS within the slipping area is poorly constrained because it is highly dependent on slip gradients, therefore, sensitive to the smoothing parameters used in the inversion.

4. Kinematic analysis of the SSE associated with the 2023 Swarm

4.1. Spatio-temporal evolution of the aseismic slip associated with the swarm

The 2023 seismic swarm starts on August 26$^{\text{th}}$ and lasts about 6 weeks, ending in early October. The SSE lasts as long as the seismic swarm and takes place in two phases, each lasting approximately 3 weeks. Overall, the total slip distribution extends over about 100 km, from 27° S to 28° S. We find an equivalent Mw 6.1 using a shear modulus of 30 GPa. The first phase is associated with a patch of slip located in the northern half of the total cumulative slip (∼27.25° S), representing an equivalent Mw 5.9. The second phase is associated with a southward propagation which results in a second patch of slip reaching an equivalent Mw 5.7 in the southern half of the total cumulative slip (∼27.75° S).

The spatio-temporal evolution of the SSE is constrained by GNSS coastal stations and revealed by weekly displacement rates (Fig. 3). The first snapshot corresponds to the week preceding the beginning of the seismic swarm during which no coherent motion is extracted from GNSS time series (Fig. 3-a). The resulting slip rate distribution (small, inconsistent patches of low slip) depicts the level of uncertainties associated with our inversion scheme (∼5 mm/wk). During the first week following the beginning of the swarm, very little motion is observed (Fig. 3-b). Then, larger motions

initiate in two distinct patches.
During the first half of September, the northernmost station (BING located at 27.15° S), starts to move (approximately 0.13 mm/day), while the southern stations (BAR2, TTRL, LLCH) show no movement (Fig. 3-b to d and Fig. 4, phase 1). A zone of large slip is highlighted, centered at 27.2° S (Fig. 3-d, area B). During the second half of September, the northern station slows down while southern stations (BAR2 at 27.6° S and TTRL at 28° S) start to move westward (approximately 0.05 mm/day, Fig. 4), concomitant with a decrease of slip rate in the northern zone (Fig. 3-e). By the end of the month, slip has stopped in the north, (Fig. 3-f). Conversely, slip develops in the south, resulting in up to 20 mm/week of slip rate, over an area that is actually larger than the northern zone (Fig. 3-f, zone C and Fig. 4-phase 2). By mid-October, no movement greater than the daily scatter can be extracted from the GNSS time series (Fig. 3-g and h, Fig. 4). This marks the end of the SSE.

4.2. Coulomb failure stress change and swarm seismicity rates

We analyze the locations of the four most prominent seismic clusters during the swarm (Fig. 3). Cluster 1 corresponds to the initiation of the swarm. It started during the week from 08/26 to 09/01; however, the geodetic signal during this week is too small to properly constrain slip rates (Fig. 3-b). During the following week, the cluster migrated downdip and seismicity rates increased significantly. During this period, slip rates located downdip of the seismicity reached amplitudes of 8 mm/week, and the associated positive ΔCFS at the location of the cluster reached 0.5 kPa for a minimum slip-rate threshold of 6 mm/week (Fig. 5-a). For minimum slip-rate thresholds of 4 or 5 mm/week, the cluster lies at the edge of the slipping area and the corresponding ΔCFS values become negative. This cluster continues during the following week (Münchmeyer et al., 2025c); however, the seismicity is then dominated by the Ml 5.3 event and its aftershocks, consistent with a mainshock–aftershock sequence within the cluster 1. The second cluster analyzed is located north of the cumulative slip area. The corresponding ΔCFS reached cumulative amplitudes of 6 kPa during the two weeks from 09/09 to 09/22 (Fig. 5-b). The 22 earthquakes forming this cluster all occurred during the second week. The third seismic cluster is located updip of the total slip, near the subducted seamount but slightly below the subduction interface. Both a large increase in seismicity rates and positive ΔCFS occurred during

the two weeks from 09/16 to 09/29, with 72 earthquakes and ΔCFS reaching 1.1 kPa (Fig. 5-c). The fourth cluster is located at the southern edge of the cumulative slip. ΔCFS increased during the two weeks from 09/16 to 09/29, reaching amplitudes of 1.2 kPa, although the large majority of earthquakes occurred during the following week (Fig. 5-d).

5. Discussions

5.1. Cumulative slip distribution : static versus kinematic inversions

There are two different methods for imaging the cumulative slip distribution on the fault. The most common method consists of performing a static inversion of the cumulative deformation. Another method consists of adding the successive weekly displacement rates. It is only possible if they can be quantified accurately. It is the case here, thanks to the precision in determining the weekly displacements. Both slip distributions highlight slip over the same area of about 100 km, between 27 and 28° S (Fig. 6). They also exhibit similar first-order characteristics, such as slip amplitude, location of local maxima, for the same quality of fit to the data. The difference lies in the details of the slip distribution. The cumulative kinematic slip distribution features two spatially disconnected patches of maximum slip (∼up 30 mm), which are constrained by the desynchronized motion of coastal stations (Fig. 6-A). In contrast, the static slip inversion exhibits a single patch of maximum slip, with a smaller amount of slip to the south (Fig. 6-B). Details of the slip history taken on specific nodes of the geometry can be found in the Supplementary material Fig. S4. Finally, we show here that only a kinematic analysis of the transient deformation can properly reconstruct the cumulative slip of that kind of propagating event.

5.2. Impact of coastal stations

Our slip distribution appears quite different from the one published previously by Münchmeyer et al. (2025c). At first order, the event duration and the affected area are similar. However, the secondary slip patch in the south is only present in our solution. The reason for this difference lies in the presence of denser coastal stations. The amplitude and direction of the southern stations impose a quantity of slip much larger to the south than suggested by the previous study, which precisely lacks coastal stations there. To confirm that conclusion, we invert for the cumulative static slip distribution, removing observations from southern stations absent in Münchmeyer et al.

(2025c) (BAR2 and TTRL, Fig. S5). Our test shows that only the northern slip patch is recovered. Moreover, the slip distribution does not exhibit the low-amplitude slip propagating to the south depicted by Münchmeyer et al. (2025c). The reason is the absence of one station at $\sim$ 30 km from the coast around 28° S in our dataset, which detects small motion (see Fig. S6). Eventually, the reason why the southern slip they detect is less than the one depicted by our preferred slip distribution is because this station detects only 1/3 of the motion detected by northern stations, when in our dataset, southern coastal stations move as much as northern coastal stations. Their model also underpredicts the displacement of this station.

5.3. Interplay between fast and slow slip

In order to further evaluate the interplay between fast (seismic) and slow (aseismic) slip inverted from GNSS data, we compute geodetic and seismic moment rates in 3 specific areas (see Fig. 7): A corresponds to the total region of the SSE (27° to 28° S); B corresponds to the northern patch of slip and C to the southern patch. Seismic moment rates are computed from the Münchmeyer et al. (2025b) catalog, using the 'Interface seismicity'. Geodetic moment rates are computed from the slip rate distributions, using a shear modulus of 30 GPa.

The early onset of the geodetic moment rate could suggest that SSE starts before the swarm seismicity. However, this is possibly due to aliasing because of the temporal smoothing imposed by the median filter on 30-days window. Going further, according to the level of noise highlighted during the week preceding the swarm (Fig. 3-a), any slip rate below 5 mm/week, that is moment rate below $0.1e18$ N.m, should not be interpreted. This threshold of 5 mm/week is only exceeded when the seismic moment increases.

The main result is that the geodetic moment (of the order of $1e18$ N.m) is one order of magnitude larger than the seismic moment (of the order of $1e17$ N.m). Overall, the seismic moment accounts for only 7% of the geodetic moment. A second important result is the different seismo-geodetic behaviors within the two slip patches. Slip and seismicity are associated and synchronized during the first phase in the northern area B, but not in the southern area C. There, seismicity mostly occurs updip of the bulk of slip and is significantly smaller, both in number and in magnitude, than in the northern patch. There are only a few rare events of Ml$>$ 2.5 in region C (Fig. 7-C), compared to region B (Fig. 7-B).

At a finer temporal and spatial scale, ΔCFS change calculations show similar behavior across the four clusters analyzed. Seismicity clusters systematically occur at the edges of the slipping areas. Depending on the slip-rate threshold used, the seismicity is either located outside the slipping areas (minimum slip rate $>$ 6 mm/week) or at their boundaries (minimum slip rate $>$ 4–5 mm/week). For amplitudes below 6 mm/week, slip rates become poorly constrained by the onshore GNSS data and likely reflect spatial smoothing. Our interpretation is therefore that the seismic clusters occur slightly outside the slipping areas, where ΔCFS amplitudes are maximal, typically around 1-5 kPa. If the swarms were directly triggered by aseismic slip itself, they would be expected to occur at the locations of peak slip rates, which is not observed. A temporal delay between the ΔCFS and larger seismicity rates is observed at clusters 2 and 4. The cluster 4, which exhibits the longest delay, is located within the area affected by the 2020 sequence (total equivalent magnitude 7.1, Klein et al., 2021) which may have modified the loading conditions to activate this cluster. Temporal delays between ΔCFS and seismicity rates, as well as their underlying physical mechanisms, warrant further investigation.

5.4. Long-term seismicity and recurrence of the swarm activity

Over the last 20 years, 3 swarms (increase of seismicity rate without a clear mainshock earthquake, Holtkamp et al., 2011), of various sizes but always located offshore Caldera have been identified (2006, Ojeda et al. (2023); 2015, Marsan et al. (2023) and the latest one in 2023). Münchmeyer et al. (2025c) suggested that additional ones occurred in 1988, 2016, 2018, and 2020. In order to reinvestigate the recurrence of the Caldera swarms, we perform a systematic analysis of different catalogs. For the different events, we compare the number of events per day and the cumulative number of events over time, alongside the spatio-temporal evolution of seismicity (Fig. S7). We use the International Seismological Centre (ISC) catalog for the period 1964 - 2012 (Storchak et al., 2013, 2015; Di Giacomo et al., 2018). Starting in 2012, we rely on the CSN catalog (Barrientos, 2018; Potin et al., 2025) and compare it with the 2014-2024 catalog from Münchmeyer et al. (2025b). Our analysis does not call into question the swarm characterization of the 1973 and 2006 crises. The 1988 crisis exhibits behavior very similar to that of the 1979 swarm, with a low number of events and no real spatial clustering. However, high magnitude of completeness and poor location at the time make it difficult to draw a conclusion. In contrast, the 2016 crisis re-

veals a distinct spatio-temporal seismic cluster, confined to a brief period between November 30 and December 2. This event qualifies as a swarm, though it remains small in both spatial extent and earthquake magnitude - very similar to the 2015 swarm. We exclude the 2018 crisis, which does not depict any spatial clustering of earthquakes, with seismicity scattered over a relatively long period (see Fig. S7). Similarly, the 2020 crisis is dismissed due to its clear mainshock-aftershock pattern, showing exponential decay in the number of events and magnitudes during the first weeks of the sequence (Figs. S7 and S8), despite the unusual occurrence of two large aftershocks (Klein et al., 2021). Although aftershock activity propagated northward - aligned with postseismic deformation - the crisis location falls outside the Caldera swarm locus (approximately 70 km south).
Swarms in this region occur in a preferential location and recur over time—1973, 1979, 2006, 2015, 2016, and now 2023. The time window in which they occur may be influenced by the magnitude of the events within each swarm (for example, the 2015 swarm consisted of very small magnitudes). However, the lack of a uniform catalog makes it difficult to infer any clear periodicity (see Fig.8-C). Nevertheless, it is noteworthy that the 2006 and 2023 swarms exhibit comparable nucleation behavior, characterized by a localized early cluster lasting 8 to 10 days and confined to a specific latitudinal range before expanding both spatially and temporally (see Fig. S9). Although the total seismic moment release during the early cluster differs (equivalent to a magnitude Mw 5.6 in 2006 and Mw 4.6 in 2023), the ratio of the early cluster moment over the swarm moment release remains similar in both cases, in the order of 0.03-0.09 depending on the catalog used.

Our analysis demonstrates that the two patches of the 2023 SSE exhibit different seismo-geodetic behaviors. Larger events are overall collocated with maximum slip in the northern patch, while microseismicity is most likely driven by distant Coulomb failure stress changes in the southern patch. In fact, long-term seismicity depicts a very similar behavior (Figs. 8 and S10). We found earthquakes located within the northern area of maximum slip of the 2023 SSE during almost all past swarms (Fig. 8-B, C northern patch). In contrast, the long-term seismicity clearly depicts a very low level of activity within the southern patch of slip (Fig. S10), with no events associated with past swarms in the maximum slip zone (Fig. 8-B, C southern patch). The southernmost part of that section ($\sim$28° S) is dominated by sequences such as those of December 2011 (see Fig. S1 from Ojeda et al., 2023) or September 2020 (Klein et al., 2021).

5.5. Effect of the subducted Copiapó Ridge

The subduction of the Copiapó Ridge is considered a key factor influencing the mechanical behavior of the megathrust (Pastén-Araya et al., 2022; Ojeda et al., 2023; Molina-Ormazabal et al., 2025). The ridge consists of volcanic seamounts on the incoming Nazca Plate (Fig. 1) that locally thicken and structurally modify the oceanic crust prior to subduction (Warwel et al., 2025). In addition, the rough topography associated with seamounts enhances fracturing of the incoming plate, reactivating pre-existing faults and generating new bending-related normal faults that act as pathways for seawater penetration into the oceanic crust. This fluid infiltration promotes hydration reactions, increasing the fluid content of the slab as observed with high V_p/V_s ratios (Pastén-Araya et al., 2022). These structural and compositional heterogeneities are therefore expected to modify the stress field and favor conditionally stable frictional behavior.

Observations of seismicity and interseismic coupling reveal strong spatial variability, with seismicity often concentrated in relatively well-coupled regions and reduced in areas interpreted as weakly coupled (Fig. 8). This variability is consistent with the interaction between the subducted ridge and the megathrust, where seamount relief perturbs the stress field, locally concentrating stress while generating adjacent stress shadows that promote distributed or aseismic deformation. Recent studies further suggest that, in the Copiapó region, seismic swarms are closely linked to slow slip processes, with evidence that the 2006 swarm involved a combination of seismic and aseismic slip driven by the subduction of ridge-related seamounts (Ojeda et al., 2023; Münchmeyer et al., 2025c; Warwel et al., 2025). These observations indicate that ridge subduction facilitates the partitioning of deformation into both seismic and aseismic modes.

Similar associations between subducted seamounts, shallow slow slip events, and seismic swarms have been documented in other subduction zones, including the Hikurangi margin offshore Gisborne and Hawke's Bay in New Zealand (Todd et al., 2018; Shaddox and Schwartz, 2019; Bangs et al., 2023), the Nankai Trough off the Kii Peninsula (Flores et al., 2025), and the Ecuador subduction zone (Segovia et al., 2018). Together, these observations support the interpretation that subducted seamounts and ridges play a fundamental role in promoting the coexistence of seismic swarms and slow slip along subduction interfaces.

5.6. Bimodal behavior of the fault within the LCZ

The different behaviors highlighted by both the 2023 seismic swarm and the associated SSE, actually reveal different frictional characteristics of the fault at quite small scale, which appears very consistent with our coupling model (See Fig. 8-A, Klein et al., 2018b). In the northern area of the LCZ (between 27 and 27.5° S), this model reveals rather high coupling on a patch smaller than 50x50 km^2 surrounded by lower coupling. The 2023 swarm initiated precisely in this area, which hosted all known swarms (Fig. 8-B and C northern profile). In this same area, we also observe occasional earthquakes of magnitude up to 6 (see Fig. S11), which is not surprising given the rather high coupling. We can speculate that an earthquake of magnitude greater than 7 is unlikely to nucleate within this small highly coupled pocket, but the deformation that accumulates here is released by regular swarms associated with SSEs, as well as occasional Mw 6 earthquakes(ie, the stress-shadow effect, Métois et al., 2016).

In the southern area of the LCZ, microseismicity, significantly lower in amplitude and number than that observed in the north, is poorly collocated with aseismic slip during 2023, and most likely driven by Coulomb failure stress change (Figs. 5 and 7). This particular behavior had not been observed before, but we cannot rule out the possibility that the previous swarms developed in this southern region in a similar way to the 2023 Caldera swarm. It could be a simple instrumental threshold issue because geodetic and seismological networks have only been densified over the last 5 to 8 years. Going further, the southern SSE slip patch takes place within the shallow low coupling area. Notably, the postseismic deformation following the 2020 sequence also propagated in that area (Klein et al., 2021). The long-term seismic activity is also much lower in the southern patch of the 2023 swarm, where no earthquake magnitude larger than 5 has occurred over the last 30 years (see Fig. S11). Therefore, this area seems prone to aseismic slip, whether slip is spontaneous (SSEs) or driven by an event at its edge (e.g., the 2020 sequence).

Other coupling models exhibit much less detail of the LCZ. Due to the scarcity of the employed data (González-Vidal et al., 2023) or specific regularization methods (Yáñez-Cuadra et al., 2022), they depict a smooth LCZ, within which there is no distinction between the northern and southern areas (see the different models on Fig. S12). In contrast, the slip distribution presented here and our coupling model Klein et al. (2018b) were obtained using observations made on very consistent networks as coastal observations were

made at the same location (survey sites transformed into permanent stations, Klein et al., 2023). We are therefore confident that the SSE associated with the 2023 swarm actually reveals spatio-temporal details of the LCZ.

6. Conclusions

The Barranquilla LCZ was imaged with dense survey measurements during the steady interseismic state (Métois et al., 2014; Métois et al., 2016; Klein et al., 2018b). It had been identified as hosting many different slip modes (Klein et al., 2018a, 2021; Marsan et al., 2023; Ojeda et al., 2023; Münchmeyer et al., 2025c; Molina-Ormazabal et al., 2025). This work shows that each of these slip modes takes place in a particular area of the LCZ, indicating variable frictional behavior within this LCZ.

This study demonstrates that a GNSS network, although less dense but well located with respect to a particular event, is capable not only of detecting very small events (5 mm of surface deformation in a few weeks) but also of studying its kinematics in great detail. Investigating this kinematic is important because it provides information on the size of asperities on the interface. Our study images several small slip patches, whereas static studies image a single one. The cumulative slip for a given event is therefore different when viewed kinematically or statically, which could imply different physics. Seismic swarms regularly release the deformation accumulated within small locked asperities inside the LCZ, and the associated SSE then propagates within the area of lowest coupling. Therefore, this area may slide easily and extensively, either spontaneously or in response to the occurrence of a significant earthquake to the north or south, such as the 2020 sequence and its very large postseismic deformation. Local seismic clusters within the swarm are located at the edges of slip areas, likely triggered by Coulomb stress changes. This work supports the presence, location and precise extension of the LCZ suggested by our coupling model, in particular the presence of a shallow very low coupled area, which creeps with little to no seismicity (Fig. 8). That same area appears to coincide with the northern boundary of the 1922 earthquake (Vigny et al., 2024). One might suggest that a future major rupture of the 1922 gap could be stopped at the same location.
Because observation networks were largely undeveloped during the past swarms of 2006 and 2015, it is not possible to further investigate or draw conclusions about similarities with the 2023 one, either geodetically or seismically. However, the comprehensive analysis of this latest occurrence revealed

a very peculiar interplay between seismicity and aseismic slip that clearly calls into question the classification of *swarm*, adopted based on previous occurrences. Provided dense permanent observations can be maintained over time, the future swarm occurrences, deep SSEs and seismic sequences in this active region, will be essential to further explore, on one hand, the stability of the frictional behavior of the LCZ through the seismic cycle and on the other hand, a more specific and appropriate classification of these events.

Acknowledgments

This work was performed with financial support of the Institut National des Sciences de l'Univers (INSU-CNRS) Tellus program, the Agence Nationale de la Recherche (project ANR-19-CE31-0003). JO acknowledges the support of the EASER (Evolution Assessment of Seismic Risk) project under grant number ACT240044 from the National Agency for Research and Development (ANID). SR and JCB thanks ANID/FONDECYT, projects no. 1240501 and no. 1262157. We would like to warmly thank all CSN staff, for their precious help for the fieldwork. All the maps have been made using Generic Mapping Tools GMT (Wessel et al., 2013). Python tool-boxes used: PYACS+ PYEQ ((Nocquet and Tran, 2025) and https://github.com/JMNocquet/pyacs36), CSI (http://www.geologie.ens.fr/ jolivet/csi). The redaction in english was improved using *DeepL*.

Data availability: All time series of continuous GNSS data used in this study come from the *SOAM_ GNSS_ solENS_ V5.0* database (see repository access on Klein et al., 2022) and the latest solution (V6.0 in IGS2020) is distributed through the Geodesy Plotter (Klein, 2025).

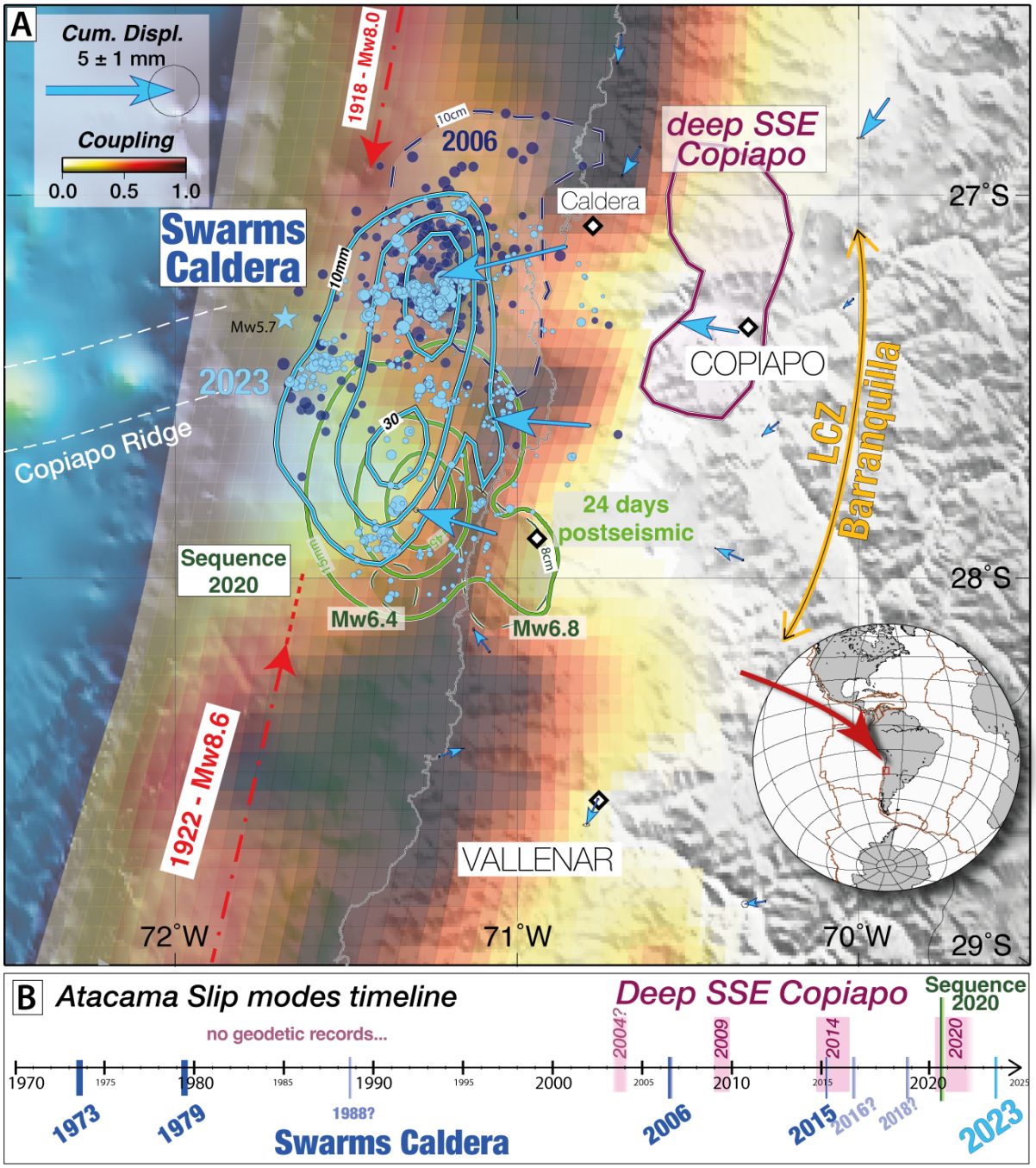
A
Cum. Displ.
5 ± 1 mm
Coupling
0.0 0.5 1.0
1918 - Mw8.0
10cm
2006
deep SSE
Copiapo
Caldera
27°S
Swarms
Caldera
10mm
Mw5.7
2023
COPIAPO
LCZ
Barranquilla
Copiapo Ridge
30
24 days
postseismic
Sequence
2020
15mm
8cm
28°S
Mw6.4
Mw6.8
1922 - Mw8.6
VALLENAR
72°W
71°W
70°W
29°S
B
Atacama Slip modes timeline
Deep SSE Copiapo
Sequence
2020
no geodetic records...
2004?
2009
2014
2020
1970
1975
1980
1985
1990
1995
2000
2005
2010
2015
2020
2025
1973
1979
1988?
Swarms Caldera
2006
2015
2016?
2018?
2023

Figure 1: **2023 swarm and seismo-tectonic context of the Atacama region.** A. The 2023 swarm is represented in light blue. Vectors depict the horizontal cumulative displacements measured between mid-August and mid-October 2023. Contours depict the cumulative kinematic slip distribution obtained in this study. Dots represent the seismicity from (Münchmeyer et al., 2025c). The blue star depicts the Mw 5.7, loc. acc. to CSN. The 2006 swarms is represented in dark blue, with the seismicity and the associated coseismic rupture zone (10 cm contour from (Ojeda et al., 2023)); The yellow-to-black color scale depicts the coupling from (Métois et al., 2016) south of 28.5° S and (Klein et al., 2018b) north of 28.5° S . The pink area inland depict the overall surface of the recurrent deep Slow Slip Event (Klein et al., 2018a, 2023). The dark green contours depict the coseismic rupture zones of the 2020 Totoral sequence (8 cm slip contour), and the light green contours the 24-days postseismic rupture zone (+15 mm contours) (Klein et al., 2021). 1922 and 1918 earthquakes rupture extension from (Vigny et al., 2024) Inset: localization of the Atacama region. B. Timeline of each known event of the 3 classes of slip modes described in our study: Caldera swarms (blue), Copiapó deep SSE (pink) and seismic/aseismic sequence of Totoral (green)

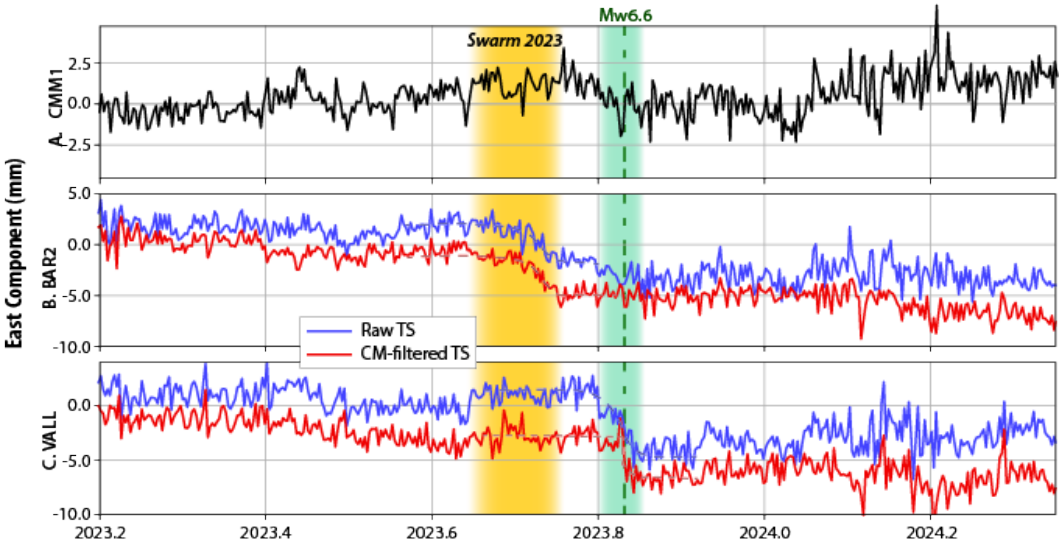

Figure 2: **Common mode correction of the GNSS times series**, illustrated on the east components, with A) CMM1 (see section 3 for common mode description); B) time series of station BAR2 located nearby the swarm and C) time series of station VALL located further south (28.5° S). For and C, the blue curve represents the raw time series and the red curve the time series corrected from the common mode. The same on the 3 components can be found in the Supplementary materials, Fig. S1

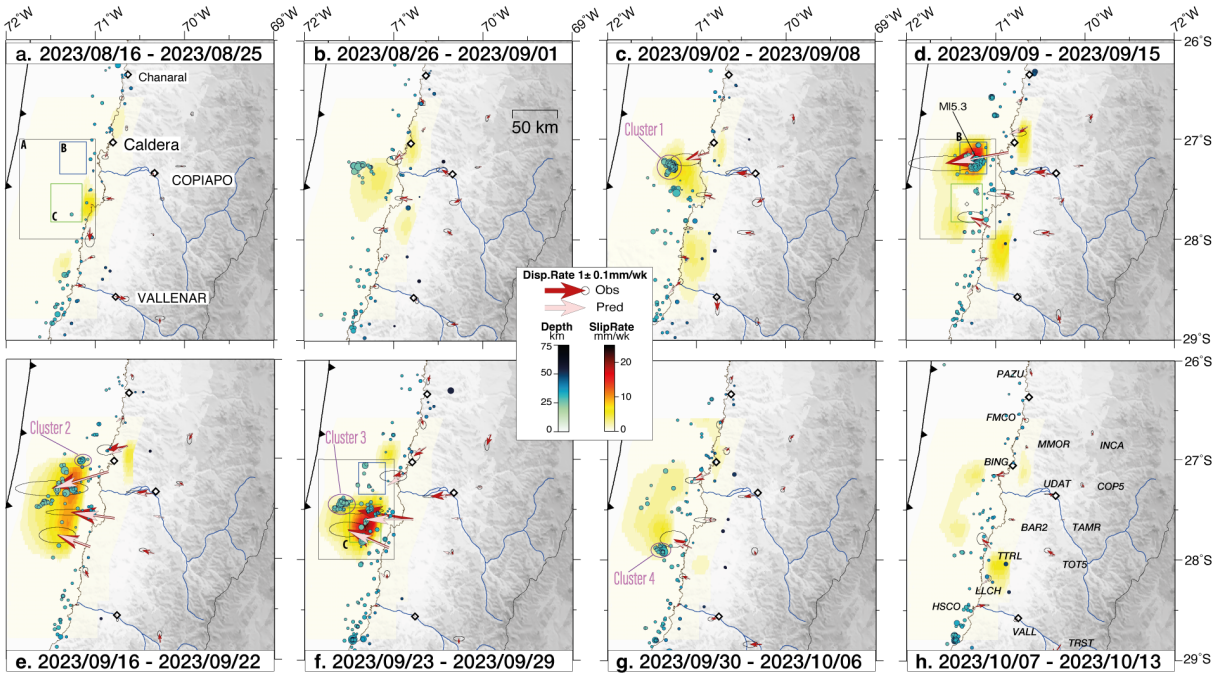

Figure 3: **Weekly snapshots of the swarm**. On each map, the weekly seismicity is extracted from (Münchmeyer et al., 2025b, , 'Interface' seismicity only), represented with the blue color scale function of depth. Red vectors depict the estimated displacement rates, the pink vectors depict displacement rates predicted by the slip rate distributions represented by the yellow to red color scale. The first snapshot depicts the week before the swarm. Areas A, B and C identified on subplot a) refers to section 5.3 and Fig.7

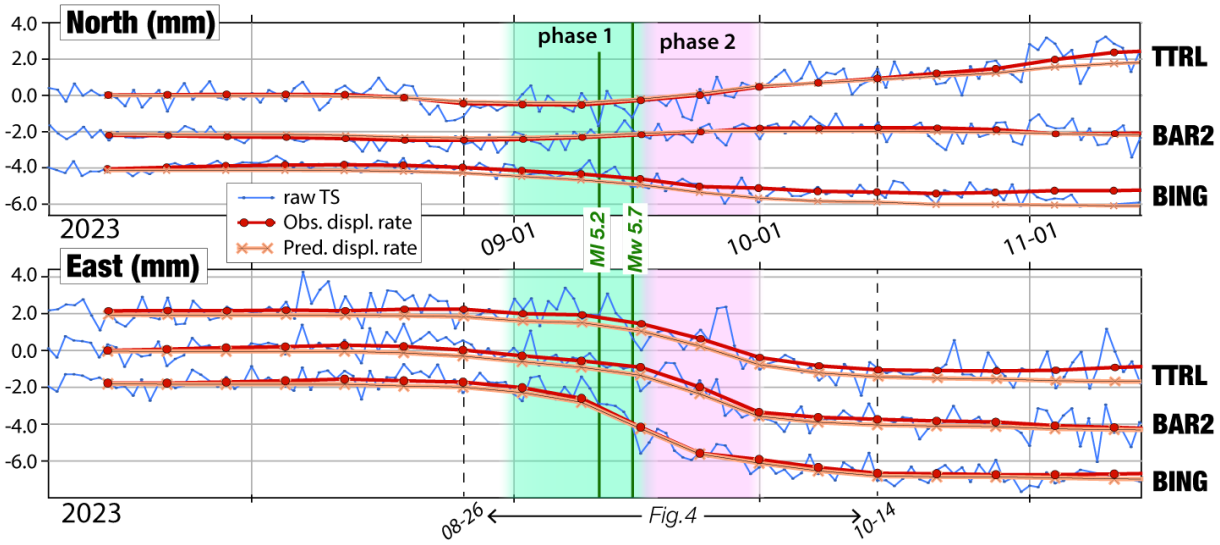

Figure 4: Comparison of the displacement rates and observed (red) vs predicted (orange) by the weekly slip rate distributions, for the 3 coastal stations TTRL, BAR2 and BING (see loc. on Fig. 3), on the north (top) and east (bottom) components. The common-mode corrected time series is represented in blue.

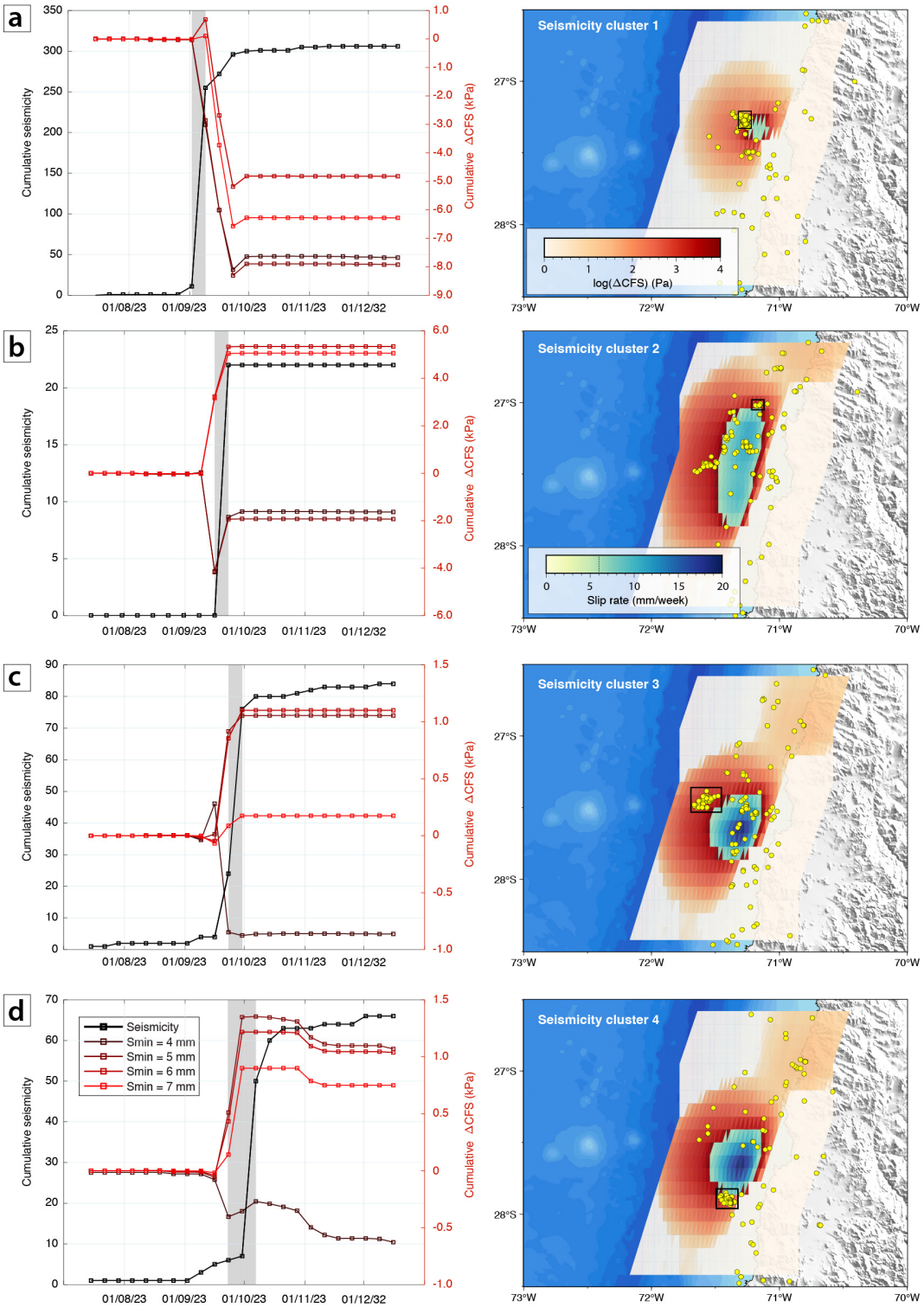
a
b
c
d
Cumulative seismicity
Cumulative ΔCFS (kPa)
01/08/23
01/09/23
01/10/23
01/11/23
01/12/32
Seismicity
Smin = 4 mm
Smin = 5 mm
Smin = 6 mm
Smin = 7 mm
Seismicity cluster 1
Seismicity cluster 2
Seismicity cluster 3
Seismicity cluster 4
log(ΔCFS) (Pa)
Slip rate (mm/week)
27°S
28°S
73°W
72°W
71°W
70°W

Figure 5: **Aseismic-slip-induced Coulomb failure stress changes and cumulative seismicity within clusters.** Left panels: Black curves show the cumulative seismicity within the black rectangles indicated on the corresponding maps to the right. Brown-to-red curves show the cumulative Coulomb failure stress change induced by aseismic slip within the same rectangles. The color depends on the minimum slip-amplitude threshold applied to the weekly aseismic slip rates. Right panels: Weekly aseismic slip rates larger than 6 mm/week are shown using the green-to-blue color scale. The associated Coulomb failure stress changes on the plate interface are shown on a logarithmic scale using the orange-to-red color scale. Yellow dots indicate seismicity. The time periods represented on the maps are indicated by the gray boxes in the left panels. Note that, for cluster 4 (d), the slip rates and Coulomb stress changes correspond to the first week, whereas the seismicity corresponds to the second week of the gray box.

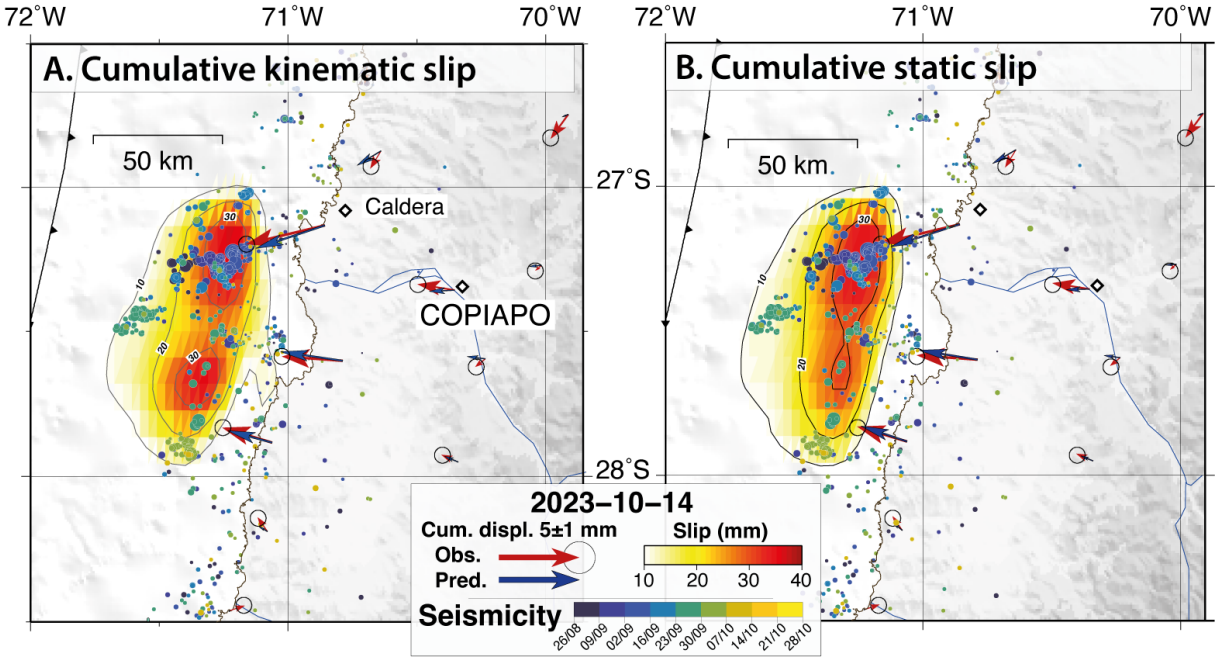

Figure 6: **Cumulative slip distributions on October, 14$^{\text{th}}$, 2023** from A. Cumulative static slip inversion and B. Cumulative kinematic slip inversion represented, both are with the same color scale. Vectors depicts cumulative displacements observed (red) VS predicted (blue). The seismic catalog from Münchmeyer et al. (2025c) is represented as function of time between August 26$^{\text{th}}$ and October 14$^{\text{th}}$.

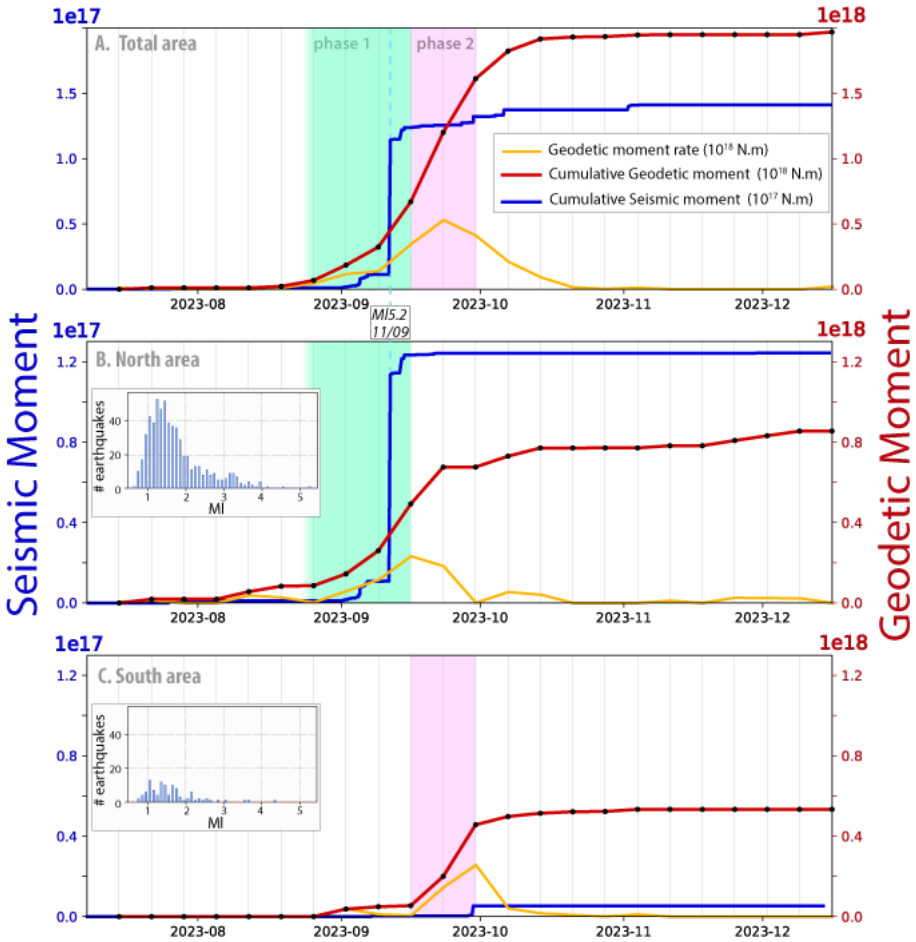

Figure 7: **Comparison of seismic VS geodetic moment evolution during the swarm**. Cumulative geodetic moment (red, scale on the right y-axis), seismological (blue, scale on the left y-axis) moment from (Münchmeyer et al., 2025b). Weekly geodetic moment rate (yellow). Moments and moment rate are computed in 3 areas (same for geodetic and seismic), depicted on Fig. 3: the total area (A), the northern patch (B), and the southern patch (C). The earthquake count as a function of magnitude (Ml) is depicted for areas B and C.

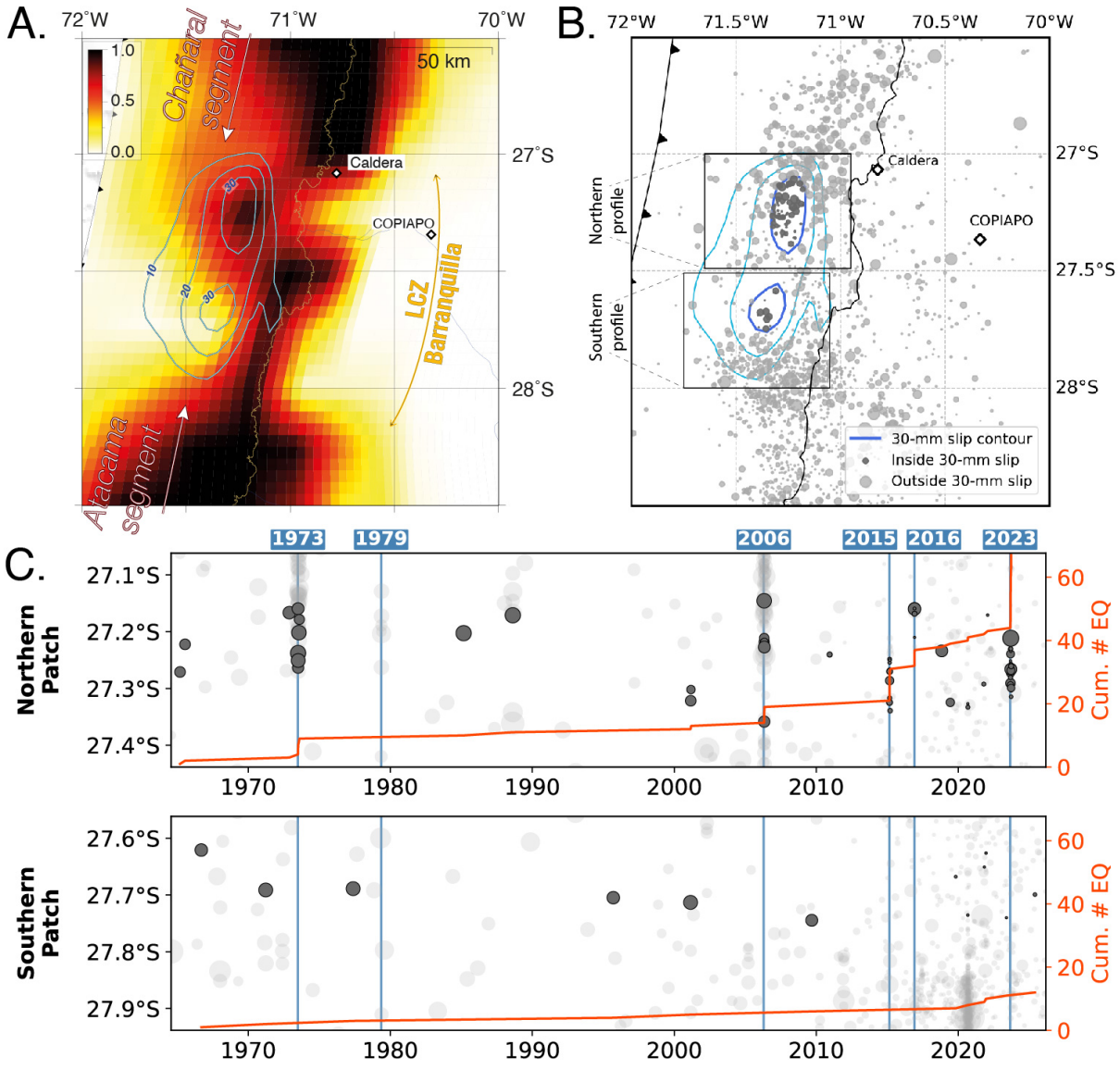

Figure 8: **Comparison of the swarm slip distribution with coupling and long-term seismicity**. A. Coupling map and segmentation from Klein et al. (2018b); B. Long-term seismicity from the ISC catalog before 2012 and the CSN catalog after 2012; C. Long-term seismicity as a function of time in the northern patch (top) and the southern patch (bottom). Dates of known swarms are depicted by the blue vertical lines. The cumulative number of earthquakes is represented by the red curve. In B and C, seismicity located directly within the 30 mm slip area of the swarm is depicted in dark gray, and seismicity outside this zone is depicted in transparent gray.

References

Báez, J., Leyton, F., Troncoso, C., del Campo, F., Bevis, M., Vigny, C., Moreno, M., Simons, M., Kendrick, E., Parra, H., et al., 2018. The Chilean GNSS network: Current status and progress toward early warning applications. Seismological Research Letters .

Bangs, N.L., Morgan, J.K., Bell, R.E., Han, S., Arai, R., Kodaira, S., Gase, A.C., Wu, X., Davy, R., Frahm, L., et al., 2023. Slow slip along the hikurangi margin linked to fluid-rich sediments trailing subducting seamounts. Nature Geoscience 16, 505–512.

Barrientos, S., 2018. The seismic network of chile. Seismological Research Letters 89, 467–474. URL: http://dx.doi.org/10.1785/0220160195, doi:10.1785/0220160195.

Beck, S., Barrientos, S., Kausel, E., Reyes, M., 1998. Source characteristics of historic earthquakes along the central Chile subduction zone. Journal of South American Earth Sciences 11, 115–129.

Boudin, F., Bernard, P., Meneses, G., Vigny, C., Olcay, M., Tassara, C., Boy, J., Aissaoui, E., Métois, M., Satriano, C., et al., 2022. Slow slip events precursory to the 2014 iquique earthquake, revisited with long-base tilt and gps records. Geophysical Journal International 228, 2092–2121.

Boulze, H., Fleitout, L., Klein, E., Vigny, C., 2022. Post-seismic motion after 3 chilean megathrust earthquakes: A clue for a linear asthenospheric viscosity. Geophysical Journal International 231, 1471–1478.

Bruhat, L., Segall, P., 2016. Coupling on the northern cascadia subduction zone from geodetic measurements and physics-based models. Journal of Geophysical Research: Solid Earth 121, 8297–8314.

Caballero, E., Chounet, A., Duputel, Z., Jara, J., Twardzik, C., Jolivet, R., 2021. Seismic and aseismic fault slip during the initiation phase of the 2017 mw= 6.9 valparaíso earthquake. Geophysical research letters 48, e2020GL091916.

Carvajal, M., Cisternas, M., Gubler, A., Catalán, P., Winckler, P., Wesson, R., 2017. Reexamination of the magnitudes for the 1906 and 1922 Chilean

earthquakes using Japanese tsunami amplitudes: Implications for source depth constraints. Journal of Geophysical Research: Solid Earth .

Di Giacomo, D., Engdahl, E.R., Storchak, D.A., 2018. The isc-gem earthquake catalogue (1904–2014): status after the extension project. Earth System Science Data 10, 1877–1899.

Dixon, T.H., Jiang, Y., Malservisi, R., McCaffrey, R., Voss, N., Protti, M., Gonzalez, V., 2014. Earthquake and tsunami forecasts: Relation of slow slip events to subsequent earthquake rupture. Proceedings of the National Academy of Sciences 111, 17039–17044.

Flores, P.C.M., Kodaira, S., Kimura, G., Shiraishi, K., Nakamura, Y., Fujie, G., No, T., Kaiho, Y., 2025. Multiple seamount subduction and lithological variability possibly control pore fluid pressure and shallow slow earthquake activity in nankai trough off muroto. Geochemistry, Geophysics, Geosystems 26, e2024GC011926.

Gombert, B., Duputel, Z., Shabani, E., Rivera, L., Jolivet, R., Hollingsworth, J., 2019. Impulsive source of the 2017 mw= 7.3 ezgeleh, iran, earthquake. Geophysical research letters 46, 5207–5216.

González-Vidal, D., Moreno, M., Sippl, C., Baez, J.C., Ortega-Culaciati, F., Lange, D., Tilmann, F., Socquet, A., Bolte, J., Hormazabal, J., et al., 2023. Relation between oceanic plate structure, patterns of interplate locking and microseismicity in the 1922 atacama seismic gap. Geophysical Research Letters 50, e2023GL103565.

Graham, S.E., DeMets, C., Cabral-Cano, E., Kostoglodov, V., Walpersdorf, A., Cotte, N., Brudzinski, M., McCaffrey, R., Salazar-Tlaczani, L., 2014. Gps constraints on the 2011–2012 oaxaca slow slip event that preceded the 2012 march 20 ometepec earthquake, southern mexico. Geophysical Journal International 197, 1593–1607.

Hayes, G.P., Moore, G.L., Portner, D.E., Hearne, M., Flamme, H., Furtney, M., Smoczyk, G.M., 2018. Slab2, a comprehensive subduction zone geometry model. Science 362, 58–61.

Herring, T., King, R., McClusky, S.C., 2010a. GAMIT : GPS Analysis at MIT, release 10.71.

Herring, T., King, R., McClusky, S.C., 2010b. GLOBK : Global Kalman filter VLBI and GPS analysis program release 10.71.

Holtkamp, S.G., Pritchard, M.E., Lohman, R.B., 2011. Earthquake swarms in South America. Geophysical Journal International 187, 128–146. doi:10.1111/j.1365-246X.2011.05137.x.

Husen, S., Kissling, E., Flueh, E., Asch, G., 1999. Accurate hypocentre determination in the seismogenic zone of the subducting Nazca Plate in northern Chile using a combined on-/offshore network. Geophysical Journal International 138, 687–701.

Jolivet, R., Jara, J., Dalaison, M., Rouet-Leduc, B., Özdemir, A., Dogan, U., Çakir, Z., Ergintav, S., Dubernet, P., 2023. Daily to centennial behavior of aseismic slip along the central section of the north anatolian fault. Journal of Geophysical Research: Solid Earth 128, e2022JB026018.

Jolivet, R., Simons, M., Duputel, Z., Olive, J.A., Bhat, H., Bletery, Q., 2020. Interseismic loading of subduction megathrust drives long-term uplift in northern chile. Geophysical Research Letters 47, e2019GL085377.

Kelleher, J., 1972. Earthquakes and some predictions. Journal of Geophysical Research 77.

Klein, E., 2025. Geodesy plotter. https://www.poleterresolide.fr/geodesy-plotter/#/?bounds=-122.69531250000001,-63.15435519659187,21.26953125,27.21555620902969&solution=SOAM_GNSS_solENS.

Klein, E., Duputel, Z., Zigone, D., Vigny, C., Boy, J.P., Doubre, C., Meneses, G., 2018a. Deep transient slow slip detected by survey gps in the region of atacama, chile. Geophysical research letters 45, 12–263.

Klein, E., Métois, M., Meneses, G., Vigny, C., Delorme, A., 2018b. Bridging the gap between North and Central Chile : insight from new GPS data on coupling complexities and the Andean sliver motion. Geophysical Journal International 213, 1924 – 1933.

Klein, E., Potin, B., Pasten-Araya, F., Tissandier, R., Azua, K., Duputel, Z., Herrera, C., Rivera, L., Nocquet, J.M., Baez, J.C., et al., 2021. Interplay

of seismic and a-seismic deformation during the 2020 sequence of atacama, chile. Earth and Planetary Science Letters 570, 117081.

Klein, E., Vigny, C., Duputel, Z., Zigone, D., Rivera, L., Ruiz, S., Potin, B., 2023. Return of the atacama deep slow slip event: The 5-year recurrence confirmed by continuous gps. Physics of the Earth and Planetary Interiors 334, 106970.

Klein, E., Vigny, C., Nocquet, J.M., Boulze, H., 2022. A 20 year-long gnss solution across south-america with focus in chile. Bulletin de la Société géologique de France 193.

Loveless, J.P., Meade, B.J., 2010. Geodetic imaging of plate motions, slip rates, and partitioning of deformation in Japan. Journal of Geophysical Research: Solid Earth 115, n/a–n/a. URL: http://dx.doi.org/10.1029/2008JB006248, doi:10.1029/2008JB006248.

Loveless, J.P., Meade, B.J., 2011. Spatial correlation of interseismic coupling and coseismic rupture extent of the 2011 Mw = 9.0 Tohoku-Oki earthquake. Geophysical Research Letters 38, n/a–n/a. URL: http://dx.doi.org/10.1029/2011GL048561, doi:10.1029/2011GL048561.

Madariaga, R., Métois, M., Vigny, C., Campos, J., 2010. Central chile finally breaks. Science 328, 181–182. URL: http://dx.doi.org/10.1126/science.1189197, doi:10.1126/science.1189197.

Marsan, D., Reverso, T., Socquet, A., 2023. Earthquake swarms along the chilean subduction zone, 2003–2020. Geophysical Journal International 235, 2758–2777.

Métois, M., Vigny, C., Socquet, A., 2016. Interseismic coupling, megathrust earthquakes and seismic swarms along the Chilean subduction zone (38–18° S). Pure and Applied Geophysics 173, 1431–1449.

Métois, M., Vigny, C., Socquet, A., Delorme, A., Morvan, S., Ortega, I., Valderas-Bermejo, C.M., 2014. GPS-derived interseismic coupling on the subduction and seismic hazards in the atacama region, Chile. Geophysical Journal International 196, 644–655. doi:10.1093/gji/ggt418.

Molina-Ormazabal, D., Radiguet, M., Münchmeyer, J., Hernandez-Soto, N., Vezinet, A., Pousse-Beltran, L., Castro, C., Doin, M.p., Baez, J.C.,

Moreno, M., et al., 2025. Slip modes along a structurally-driven earthquake barrier in chile. Journal of Geophysical Research: Solid Earth 130, e2024JB030796.

Moutote, L., Itoh, Y., Lengliné, O., Duputel, Z., Socquet, A., 2023. Evidence of a transient aseismic slip driving the 2017 valparaiso earthquake sequence, from foreshocks to aftershocks. Journal of Geophysical Research: Solid Earth 128, e2023JB026603.

Münchmeyer, J., Frank, W.B., Giffard-Roisin, S., Marsan, D., Tilmann, F., Moreno, M., Socquet, A., 2025a. A systematic search for tectonic tremor and low-frequency earthquakes in the atacama segment of the chilean subduction zone turns up empty. Journal of Geophysical Research: Solid Earth 130, e2025JB031283.

Münchmeyer, J., Molina-Ormazabal, D., Marsan, D., Langlais, M., Baez, J.C., Heit, B., González-Vidal, D., Moreno, M., Tilmann, F., Lange, D., et al., 2025b. Characterizing the atacama segment of the chile subduction margin (24 s–31 s) with> 165,000 earthquakes. Journal of Geophysical Research: Solid Earth 130, e2025JB031256.

Münchmeyer, J., Molina-Ormazabal, D., Radiguet, M., Marsan, D., Baez, J.C., Ortega-Culaciati, F., Tassara, A., Moreno, M., Socquet, A., 2025c. Seismic swarms unveil the mechanisms driving shallow slow slip dynamics in the copiapó ridge, northern chile. Geophysical Research Letters 52, e2024GL113953.

Nikkhoo, M., Walter, T.R., 2015. Triangular dislocation: an analytical, artefact-free solution. Geophysical Journal International 201, 1119–1141.

Nocquet, J.M., Tran, D.T., 2025. Pyacs: Python tools for geodetic time series and gnss velocity field analysis. URL: https://zenodo.org/doi/10.5281/zenodo.14959022, doi:10.5281/ZENODO.14959022.

Nocquet, J.M., Villegas-Lanza, J.C., Chlieh, M., Mothes, P., Rolandone, F., Jarrin, P., Cisneros, D., Alvarado, A., Audin, L., Bondoux, F., et al., 2014. Motion of the continental slivers and creeping subduction in the northern Andes. Nature Geosciences doi:10.1038/NGEO2099.

Ojeda, J., Morales-Yáñez, C., Ducret, G., Ruiz, S., Grandin, R., Doin, M.P., Vigny, C., Nocquet, J.M., 2023. Seismic and aseismic slip during the 2006

copiapó swarm in north-central chile. Journal of South American Earth Sciences 123, 104198.

Oryan, B., Gabriel, A.A., Bürgmann, R.B., Calais, E., Cheng, G., Chlieh, M., Cosenza-Muralles, B., Cruz-Atienza, V.M., Dal Zilio, L., DeMets, C., et al., 2026. The coupling cloud: A community database of megathrust kinematic coupling models .

Ozawa, S., Munekane, H., Suito, H., Yarai, H., 2025. Interplate slip before, during, and after the 2024 m w 7 hyuga-nada earthquake, southwest japan. Science 388, 1401–1405.

Pastén-Araya, F., Potin, B., Azúa, K., Sáez, M., Aden-Antoniów, F., Ruiz, S., Cabrera, L., Ampuero, J.P., Nocquet, J.M., Rivera, L., Duputel, Z., 2022. Along-dip segmentation of the slip behavior and rheology of the copiapó ridge subducted in north-central chile. Geophysical Research Letters 49. URL: http://dx.doi.org/10.1029/2021GL095471, doi:10.1029/2021gl095471.

Potin, B., Ruiz, S., Aden-Antoniow, F., Madariaga, R., Barrientos, S., 2025. A revised chilean seismic catalog from 1982 to mid-2020. Seismological Research Letters 96, 484–498.

Radiguet, M., Perfettini, H., Cotte, N., Gualandi, A., Valette, B., Kostoglodov, V., Lhomme, T., Walpersdorf, A., Cano, E.C., Campillo, M., 2016. Triggering of the 2014 Mw 7.3 Papanoa earthquake by a slow slip event in Guerrero, Mexico. Nature Geoscience 9, 829.

Rolandone, F., Nocquet, J.M., Mothes, P.A., Jarrin, P., Vallée, M., Cubas, N., Hernandez, S., Plain, M., Vaca, S., Font, Y., 2018. Areas prone to slow slip events impede earthquake rupture propagation and promote afterslip. Science Advances 4, eaao6596.

Ruegg, J.C., Rudloff, A., Vigny, C., Madariaga, R., de Chabalier, J., Campos, J., Kausel, E., Barrientos, S., Dimitrov, D., 2009. Interseismic strain accumulation measured by GPS in the seismic gap between Constitucion and Conception in Chile. Physics of the Earth and Planetary Interiors , 78–85.

Ruiz, S., Aden-Antoniow, F., Baez, J., Otarola, C., Potin, B., del Campo, F., Poli, P., Flores, C., Satriano, C., Leyton, F., et al., 2017. Nucleation

phase and dynamic inversion of the mw 6.9 valparaíso 2017 earthquake in central chile. Geophysical Research Letters 44, 10–290.

Ruiz, S., Ide, S., Potin, B., Madariaga, R., 2025. Fast and slow subduction earthquakes in latin america. Annual Review of Earth and Planetary Sciences 53.

Ruiz, S., Madariaga, R., 2018. Historical and recent large megathrust earthquakes in chile. Tectonophysics , –doi:https://doi.org/10.1016/j.tecto.2018.01.015.

Salazar, D., Easton, G., Goff, J., Guendon, J.L., González-Alfaro, J., Andrade, P., Villagrán, X., Fuentes, M., León, T., Abad, M., et al., 2022. Did a 3800-year-old m w˜ 9.5 earthquake trigger major social disruption in the atacama desert? Science advances 8, eabm2996.

Segovia, M., Font, Y., Régnier, M., Charvis, P., Galve, A., Nocquet, J.M., Jarrín, P., Hello, Y., Ruiz, M., Pazmiño, A., 2018. Seismicity distribution near a subducting seamount in the central ecuadorian subduction zone, space-time relation to a slow-slip event. Tectonics 37, 2106–2123.

Shaddox, H.R., Schwartz, S.Y., 2019. Subducted seamount diverts shallow slow slip to the forearc of the northern hikurangi subduction zone, new zealand. Geology 47, 415–418.

Socquet, A., Baez, J.C., Moreno, M., Langlais, M., Team, D.T., ISTerre, G.T.S.A., RESIF, 2020. Deep-trigger temporary experiment in the subduction zone peru/chile, chile. resif-sismob). RESIF - Réseau Sismologique et géodésique Français. doi:10.15778/RESIF.XZ2020.

Socquet, A., Valdes, J.P., Jara, J., Cotton, F., Walpersdorf, A., Cotte, N., Specht, S., Ortega-Culaciati, F., Carrizo, D., Norabuena, E., 2017. An 8 month slow slip event triggers progressive nucleation of the 2014 Chile megathrust. Geophysical Research Letters 44, 4046–4053.

Storchak, D.A., Di Giacomo, D., Bondár, I., Engdahl, E.R., Harris, J., Lee, W.H., Villaseñor, A., Bormann, P., 2013. Public release of the isc–gem global instrumental earthquake catalogue (1900–2009). Seismological Research Letters 84, 810–815.

Storchak, D.A., Di Giacomo, D., Engdahl, E., Harris, J., Bondár, I., Lee, W.H., Bormann, P., Villaseñor, A., 2015. The isc-gem global instrumental earthquake catalogue (1900–2009): introduction. Physics of the Earth and Planetary Interiors 239, 48–63.

Todd, E.K., Schwartz, S.Y., Mochizuki, K., Wallace, L.M., Sheehan, A.F., Webb, S.C., Williams, C.A., Nakai, J., Yarce, J., Fry, B., et al., 2018. Earthquakes and tremor linked to seamount subduction during shallow slow slip at the hikurangi margin, new zealand. Journal of Geophysical Research: Solid Earth 123, 6769–6783.

Uchida, N., Iinuma, T., Nadeau, R.M., Bürgmann, R., Hino, R., 2016. Periodic slow slip triggers megathrust zone earthquakes in northeastern japan. Science 351, 488–492.

Vaca, S., Vallée, M., Nocquet, J.M., Battaglia, J., Régnier, M., 2018. Recurrent slow slip events as a barrier to the northward rupture propagation of the 2016 pedernales earthquake (central ecuador). Tectonophysics 724, 80–92.

Vigny, C., Klein, E., Ojeda, J., 2024. In search for the lost truth about the 1922 & 1918 atacama earthquakes in chile. Journal of South American Earth Sciences 143, 104983.

Voss, N., Dixon, T.H., Liu, Z., Malservisi, R., Protti, M., Schwartz, S., 2018. Do slow slip events trigger large and great megathrust earthquakes? Science advances 4, eaat8472.

Wallace, L.M., Rollins, C., 2024. GNSS observations of transient deformation in plate boundary zones. Elsevier. p. 83–110. URL: http://dx.doi.org/10.1016/B978-0-323-95507-2.00009-8, doi:10.1016/b978-0-323-95507-2.00009-8.

Warwel, A., Lange, D., Dannowski, A., Contreras-Reyes, E., Klaucke, I., Diaz-Naveas, J., Moreno, M., Kopp, H., 2025. Seismic structure and tectonics of the north-central chilean subduction zone along the copiapó ridge from amphibious seismic refraction tomography and local seismicity. Geochemistry, Geophysics, Geosystems 26. URL: http://dx.doi.org/10.1029/2024GC011829, doi:10.1029/2024gc011829.

Wessel, P., Smith, W.H.F., Scharroo, R., Luis, J., Wobbe, F., 2013. Generic Mapping Tools: Improved version released. Eos, Transactions American Geophysical Union 94, 409–410. URL: http://dx.doi.org/10.1002/2013EO450001, doi:10.1002/2013EO450001.

Yáñez-Cuadra, V., Ortega-Culaciati, F., Moreno, M., Tassara, A., Krumm-Nualart, N., Ruiz, J., Maksymowicz, A., Manea, M., Manea, V., Geng, J., et al., 2022. Interplate coupling and seismic potential in the atacama seismic gap (chile): Dismissing a rigid andean sliver. Geophysical Research Letters 49, e2022GL098257.

Zhu, L., Rivera, L.A., 2002. A note on the dynamic and static displacements from a point source in multilayered media. Geophysical Journal International 148, 619–627.

Zigone, D., Duputel, Z., Rivera, L., Klein, E., Vigny, C., Ruiz, S., 2019. CopiapÓ temporary deployment around copiapó, chili (resif-sismob) [dataset]. RESIF - Réseau Sismologique et géodésique Français. doi:10.15778/RESIF.9C2019.

Bimodal seismic-aseismic behavior of a weakly coupled megathrust segment revealed by kinematic analysis of a seismic swarm and slow slip event offshore Copiapó, Chile

Supplementary material

E. Klein[a,1], J. Ojeda[b], B. Rousset[c], C. Vigny[a], S. Ruiz[d], B. Potin[d], J.C. Baez[e], D. Zigone[c]

[a]*Laboratoire de géologie - CNRS UMR 8538, École normale supérieure - PSL University, Paris, France*
[b]*Departamento de Ingeniería Civil, Universidad de Concepción, Concepción, Chile*
[c]*Institut Terre et Environnement de Strasbourg, Université de Strasbourg, CNRS UMR 7063, France*
[d]*Departamento de Geofísica, Universidad de Chile, Santiago, Chile*
[e]*Centro Sismológico Nacional, Universidad de Chile, Santiago, Chile*

*Correspondence to: klein@geologie.ens.fr

Contents of Supplementary materials

1. Figures S1 to S11
2. Tables. *Upon publication, tables of weekly displacements as well as the table of cumulative displacements shown on Fig. 1 will be attached.*

1. Time series analysis

In this section, we provide extensive information on GNSS time series analysis. Figure S1 shows the common mode correction, using CMM1 (shown on the top panel), of stations BAR2 (located in the swarm region, time series represented in the middle panel) and VALL (located in the south of the Atacama region, time series represented on the bottom panel) on the three components. Fig.S3 shows the two common-mode filters tested in that study. CMM1 was estimated using the time series of the following stations, located sufficiently far from the region of interest: PEDR, PFRJ, PVCA, RODE, BTON, TOLO, MRCG, INCA, PAZU. CMM2 was estimated with the time series of all stations in the region of interest.
Figure S2 illustrates the whole post-processing applied on the time series of station BAR2, with the common mode corrected time series (represented by the blue curve), the 30-day window median filter (represented by the orange curve), and the weekly positions estimated on the median filter (represented by pink dots).

2. Cumulative slip distribution

Here, we present additional details abouth the kinematic analysis based on cumulative weekly displacements. Figure S4 shows the final cumulative slip distribution and the slip history taken at 3 specific nodes of the geometry: in the center of the northern patch (pink); in between the two patches (green), and in the center of the southern patch (orange). Figure S5 shows the cumulative kinematic slip distributions inverted with (left, corresponding to the preferred model) or without (right) the two coastal stations BAR2 and TTRL. When these two stations are absent from the inversion, the slip distribution clearly presents a single patch of slip with a larger amplitude. As explained in the main text, this slip distribution does not exhibit the low-amplitude slip propagating to the south depicted by (Münchmeyer et al., 2025b), probably due to the absence in our dataset of one station at $\sim$ 30 km from the coast around 28° S. This station, highlighted by the green rectangle on Fig.S6 extracted from Fig. S6 of Münchmeyer et al. (2025b), detects small motion. This motion is compatible with the southern patch of slip from our preferred model, but is not sufficient in the absence of the coastal stations at that latitude to correctly constrain the slip distribution.

3. Long-term seismicity and recurrence of the swarm

For all crises (1973,1979, 1988, 2006, 2015, 2016, 2018, 2020, 2023), figure S7 represents the number of earthquake per days and cumulative number of earthquakes as function of time, and S8 represents the evolution of earthquake magnitude as function of time to evaluate whether they are swarms or standard mainshock-aftershock event, over the periods identified by Münchmeyer et al. (2025b). That figure illustrates the spatio-temporal clustering of crises that are indeed characterized as swarms, i.e., 2016, in addition to those that were already characterized, i.e., 1973, 1979, 2006, 2015, and 2023 (Holtkamp et al., 2011; Marsan et al., 2023; Ojeda et al., 2023).

Figure S9 compare the spatio-temporal evolution of the 2006 and 2023 seismic swarms in order to evaluate their similarities. In Figure S10 compares the earthquake density (that is, the cumulated number of earthquakes by bins of 0.05°) on the different catalogs for which we have long-term records: ISC (1964 - 2023); B. CSN (2000 - 2025); C. USGS (1964 - 2025); D. Potin et al. (2025) (2000 - 2020); E. ISC-CSN merged catalogs (with ISC: 1964-2012; CSN: 2012-2026). Density was computed using seismicity restricted to ± 15 km distance to the (Slab2.0 geometry Hayes et al., 2018), but tests computed at ±10 or 20 km produce similar results.

4. Comparison of the published coupling models

Figure S12 compares the three coupling distributions that were published in the region of interest, plotted with the exact same color scale. From left to right: Klein et al. (2018), Yáñez-Cuadra et al. (2022) and González-Vidal et al. (2023). Both Yáñez-Cuadra et al. (2022) and González-Vidal et al. (2023) depict a local decrease in coupling around 27.5° S, contrasting with higher coupling values to the north and south at all depths. Below 20 km, the decoupling is quite pronounced, but the coupling value remains strong above 20 km, i.e., of the order of 0.7. In contrast, the coupling model from Klein et al. (2018) depicts a lower average coupling (below 0.5) over a broader ∼ 100 km zone, between 27 and 28° S. A particular structure is imaged within the LCZ, with strong contrast of coupling: very low coupling (lower than 0.3) both up-dip and downdip, and a narrow strip of higher coupling located below the coast (see Fig. 1).

References

González-Vidal, D., Moreno, M., Sippl, C., Baez, J.C., Ortega-Culaciati, F., Lange, D., Tilmann, F., Socquet, A., Bolte, J., Hormazabal, J., et al., 2023. Relation between oceanic plate structure, patterns of interplate locking and microseismicity in the 1922 atacama seismic gap. Geophysical Research Letters 50, e2023GL103565.

Hayes, G.P., Moore, G.L., Portner, D.E., Hearne, M., Flamme, H., Furtney, M., Smoczyk, G.M., 2018. Slab2, a comprehensive subduction zone geometry model. Science 362, 58–61.

Holtkamp, S.G., Pritchard, M.E., Lohman, R.B., 2011. Earthquake swarms in South America. Geophysical Journal International 187, 128–146. doi:10.1111/j.1365-246X.2011.05137.x.

Klein, E., Métois, M., Meneses, G., Vigny, C., Delorme, A., 2018. Bridging the gap between North and Central Chile : insight from new GPS data on coupling complexities and the Andean sliver motion. Geophysical Journal International 213, 1924 – 1933.

Marsan, D., Reverso, T., Socquet, A., 2023. Earthquake swarms along the chilean subduction zone, 2003–2020. Geophysical Journal International 235, 2758–2777.

Münchmeyer, J., Molina-Ormazabal, D., Marsan, D., Langlais, M., Baez, J.C., Heit, B., González-Vidal, D., Moreno, M., Tilmann, F., Lange, D., et al., 2025a. Characterizing the atacama segment of the chile subduction margin (24 s–31 s) with> 165,000 earthquakes. Journal of Geophysical Research: Solid Earth 130, e2025JB031256.

Münchmeyer, J., Molina-Ormazabal, D., Radiguet, M., Marsan, D., Baez, J.C., Ortega-Culaciati, F., Tassara, A., Moreno, M., Socquet, A., 2025b. Seismic swarms unveil the mechanisms driving shallow slow slip dynamics in the copiapó ridge, northern chile. Geophysical Research Letters 52, e2024GL113953.

Ojeda, J., Morales-Yáñez, C., Ducret, G., Ruiz, S., Grandin, R., Doin, M.P., Vigny, C., Nocquet, J.M., 2023. Seismic and aseismic slip during the 2006 copiapó swarm in north-central chile. Journal of South American Earth Sciences 123, 104198.

Potin, B., Ruiz, S., Aden-Antoniow, F., Madariaga, R., Barrientos, S., 2025. A revised chilean seismic catalog from 1982 to mid-2020. Seismological Research Letters 96, 484–498.

Yáñez-Cuadra, V., Ortega-Culaciati, F., Moreno, M., Tassara, A., Krumm-Nualart, N., Ruiz, J., Maksymowicz, A., Manea, M., Manea, V., Geng, J., et al., 2022. Interplate coupling and seismic potential in the atacama seismic gap (chile): Dismissing a rigid andean sliver. Geophysical Research Letters 49, e2022GL098257.

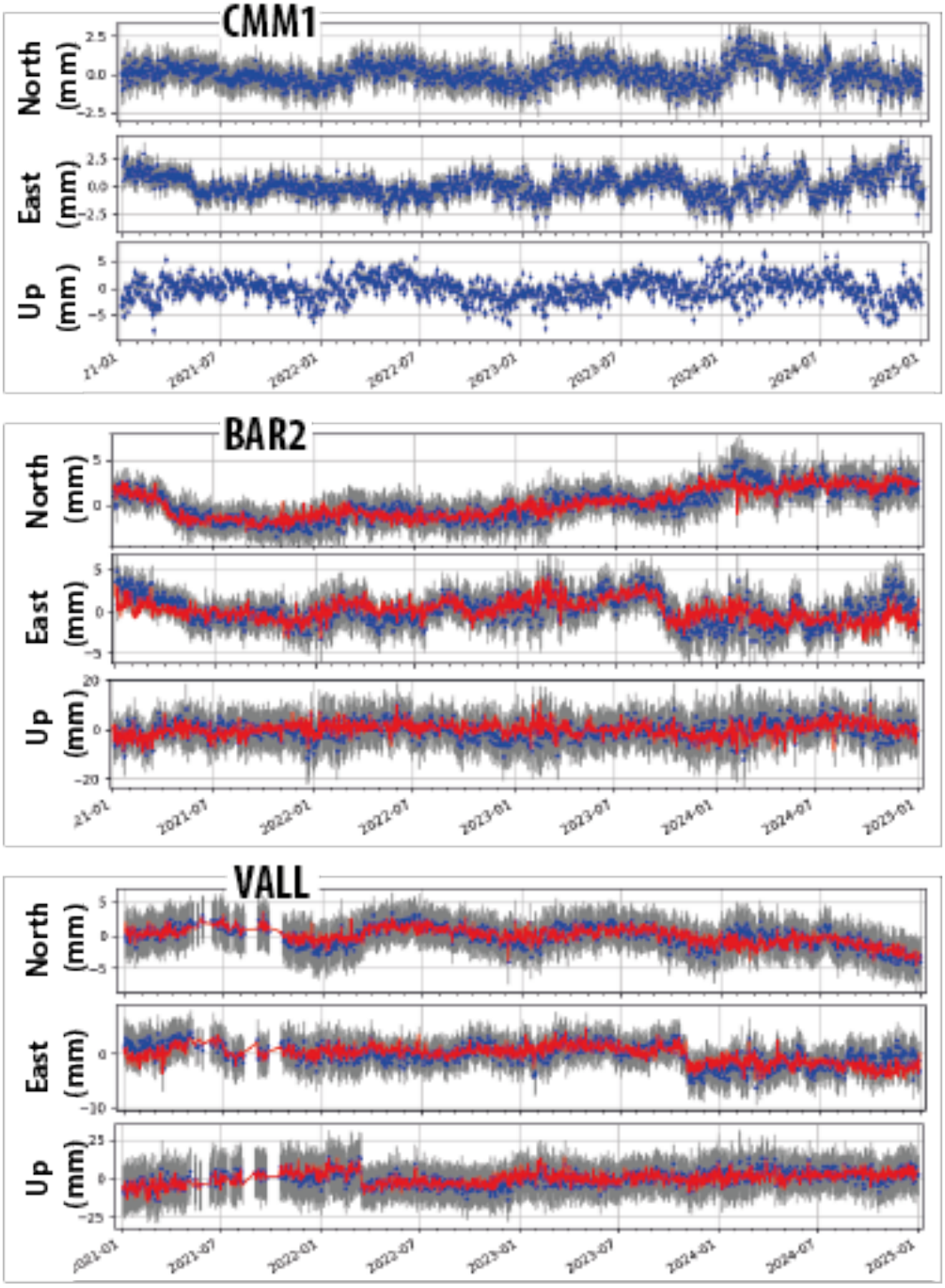

Figure S1: Common mode correction of the GPS times series on all three components. Top is the CMM1 (see section 3.1 for the list of stations used); middle is station BAR2 and down is station VALL

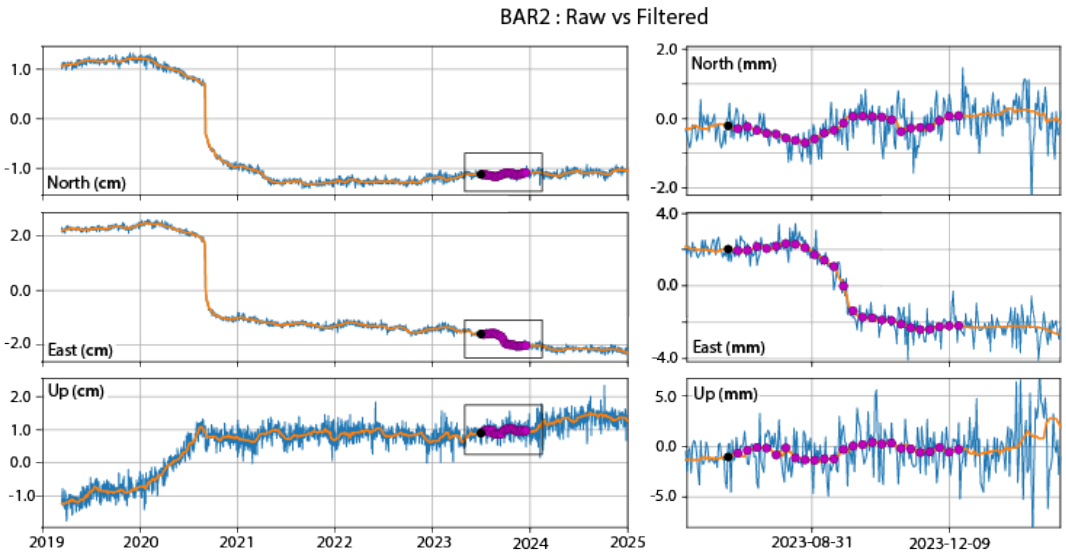

Figure S2: Time series analysis of station BAR2. The blue curves depict the common-mode-corrected GPS time series for the three components. The orange curve represents the 30-day window median filter applied to the time series. The purple dots represent the weekly positions estimated on the median filter between early July and mid-December. The left panel shows the total time series of BAR2, and the right panel focuses on the swarm period only.

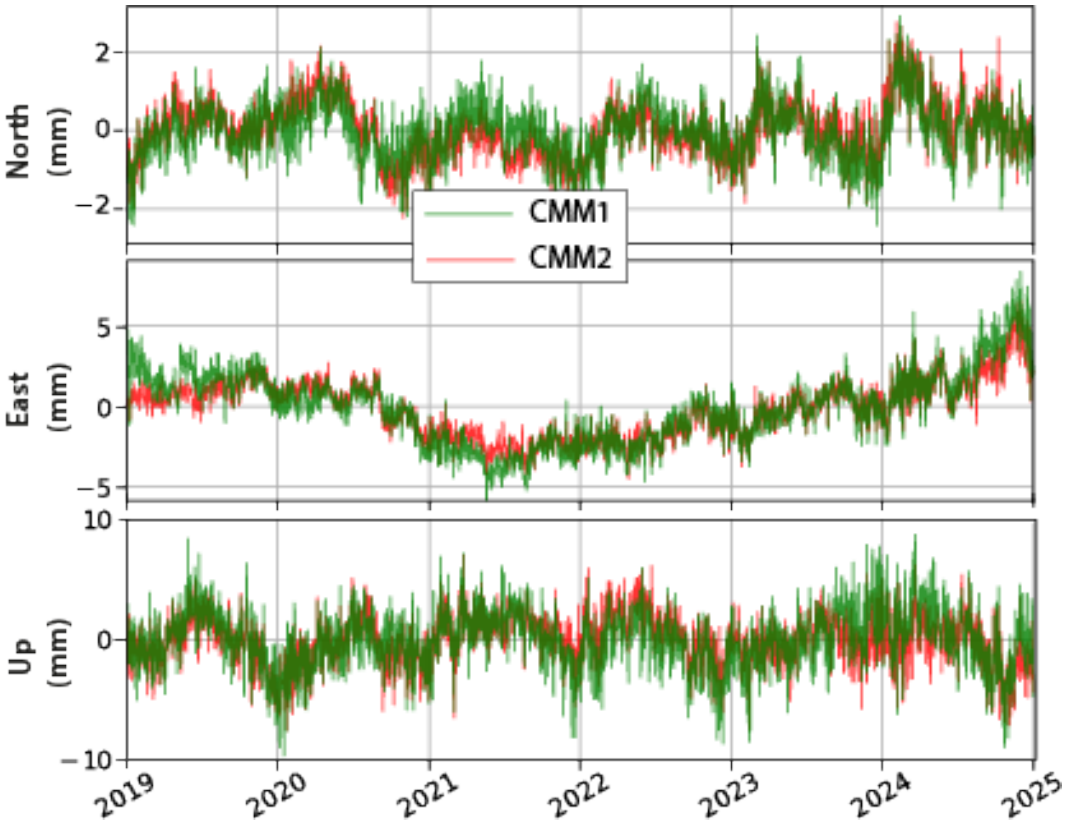

Figure S3: Comparison of the Common Modes tested: CMM1 estimated with time series of a selection of stations and CMM2 estimated with all the time series from the region.

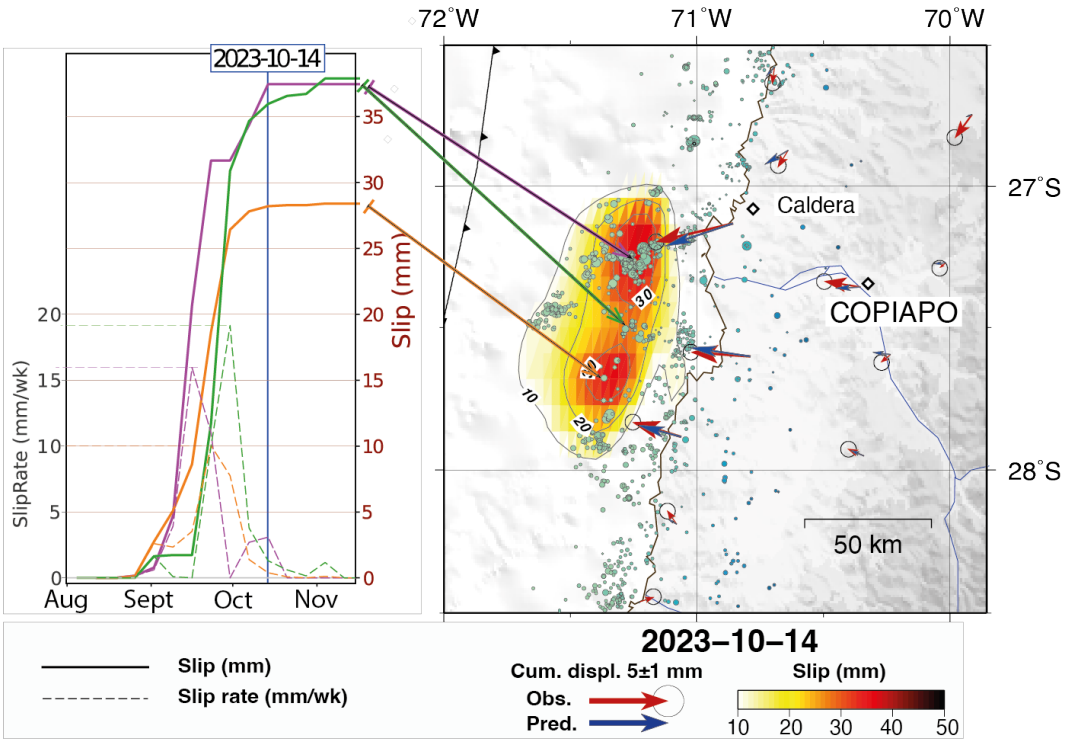

Figure S4: **Cumulative kinematic slip distributions on October 14th, 2023** same as Fig. 6. The graph depicts the slip history extracted at 3 nodes in the slip distribution geometry (violet at the north patch center, orange at the south patch center, and green at the intermediate region center). Slip (mm) as a function of time is depicted by lines, and slip rates (mm/wk) as a function of time by dashed lines.

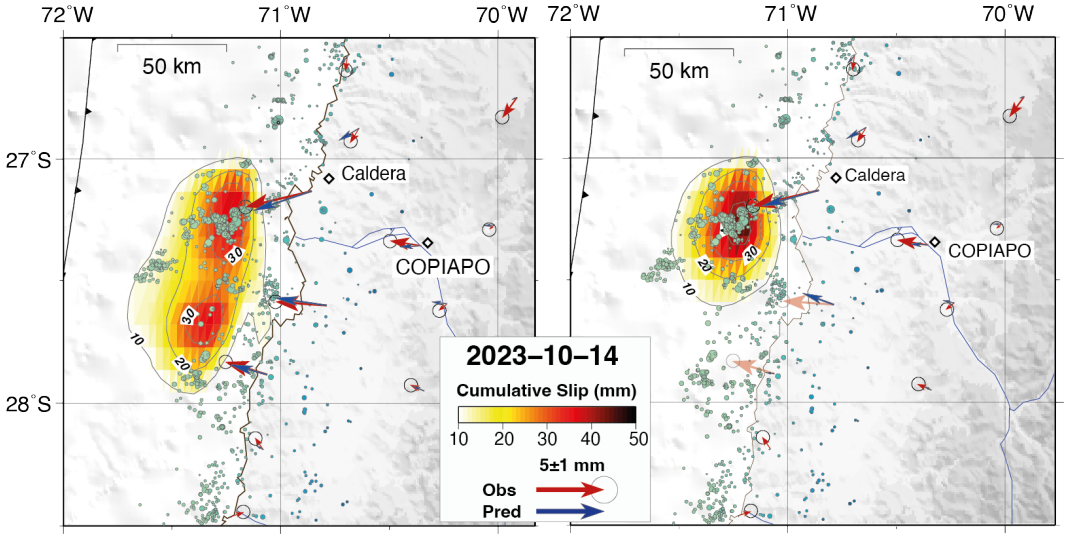

Figure S5: **Comparing cumulative slip distribution with or without coastal stations**. Left) Proposed slip distribution from this study. Right) Slip distribution inverted without BAR2 and TTRL observations. They were used to predict model displacements and are shown transparently in the figure.

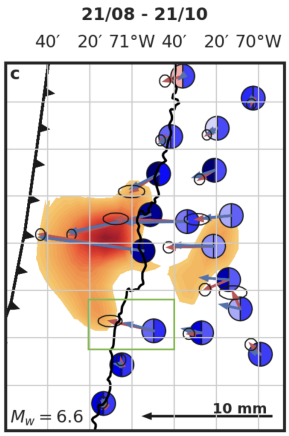

Figure S6: Extraction of Fig. S6 from Münchmeyer et al. (2025b). The green rectangle highlights the station mentioned in section 5.2.

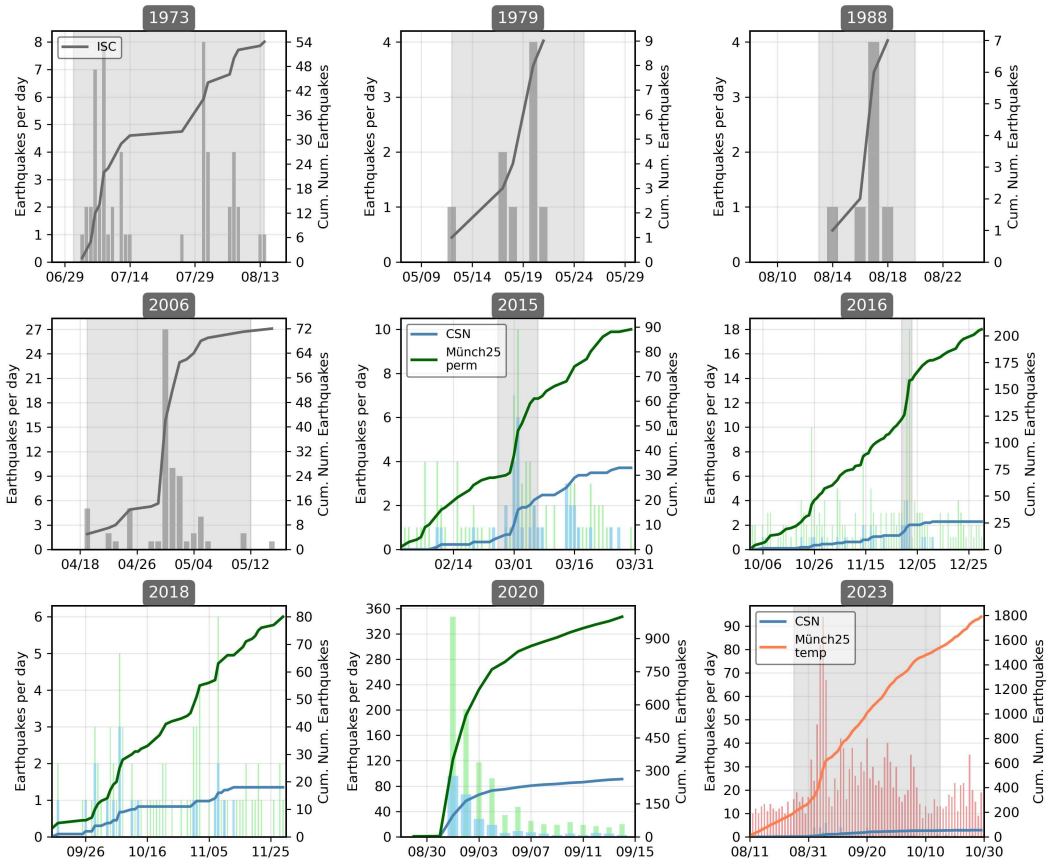

Figure S7: Revisit of past swarms using the ISC (grey), CSN (blue), and permanent (green) and temporary (red) catalogs from Münchmeyer et al. (2025a). The number of earthquakes per day (histograms) and the cumulative number of earthquakes (solid lines) are shown as functions of time. The grey area depicts the swarm period, when a swarm behavior is characterized.

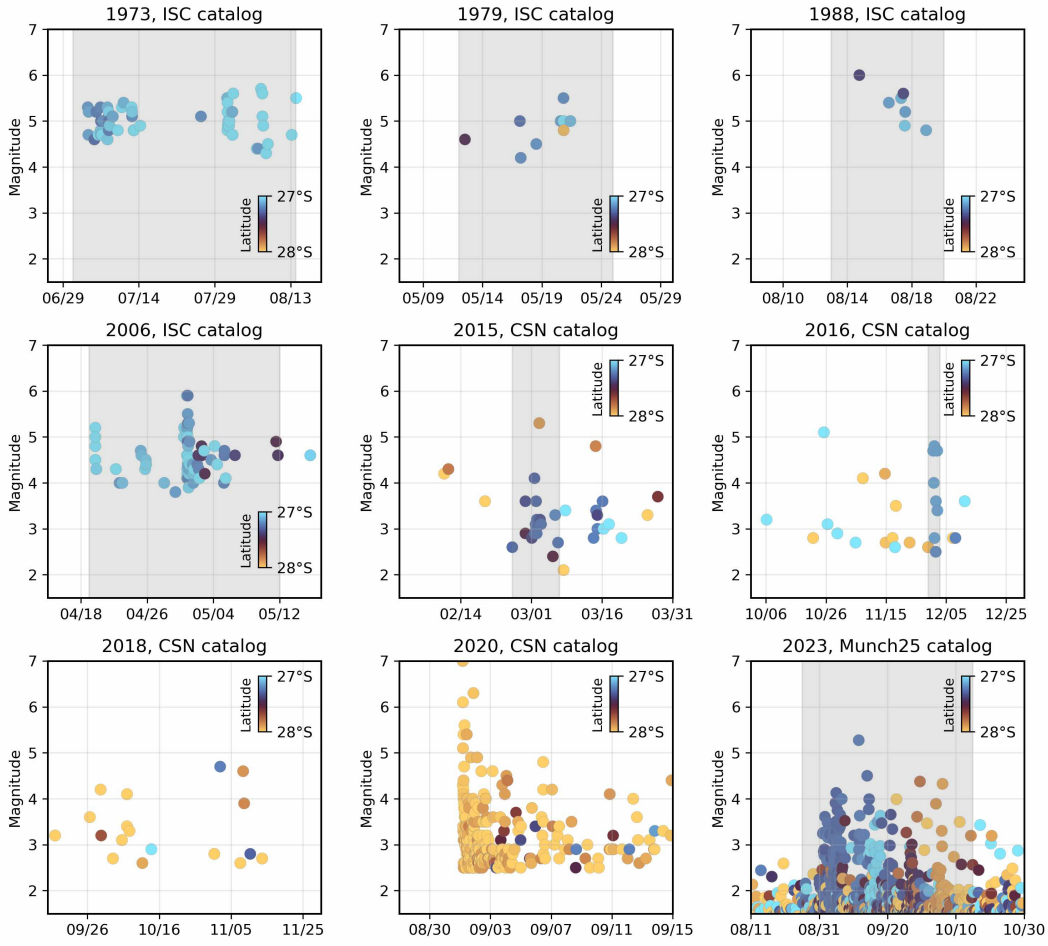

Figure S8: Revisit of past events using ICS, CSN and Münchmeyer et al. (2025b) catalogs. The magnitude is represented as a function of time, and the color scale depicts the latitude of each event in a range from 27° S to 28° S.

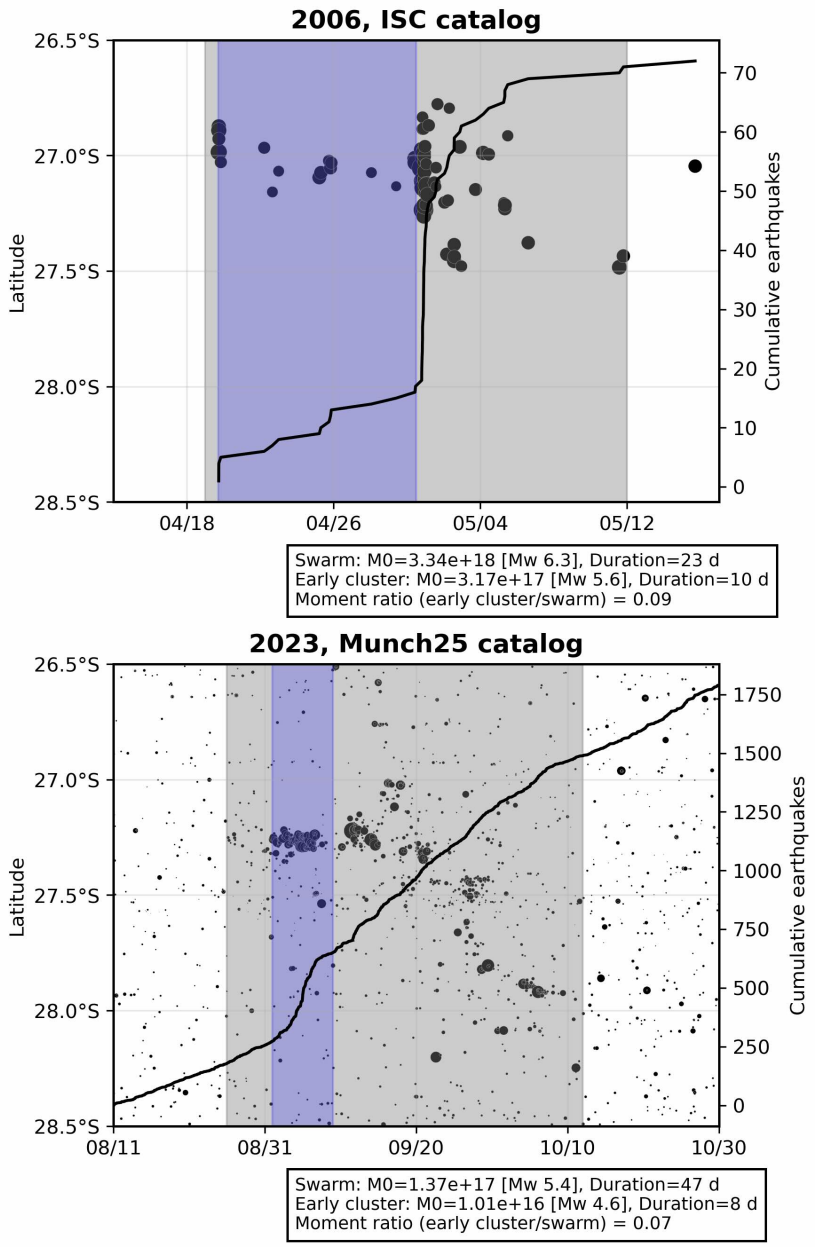

Figure S9: **Comparison of the spatiotemporal evolution of the 2006 and 2023 seismic swarms**. The blue shaded area highlights the early cluster, located near 27°S in 2006 (top panel, ISC catalog) and near 27.5°S in 2023 (bottom panel, Münchmeyer et al. (2025b) catalog). Gray shading indicates the duration of each swarm. The black curve (on the right axis) represents the cumulative number of earthquakes. Total seismic moment and duration are shown for each seismic swarm and their respective early clusters, as well as their moment ratio.

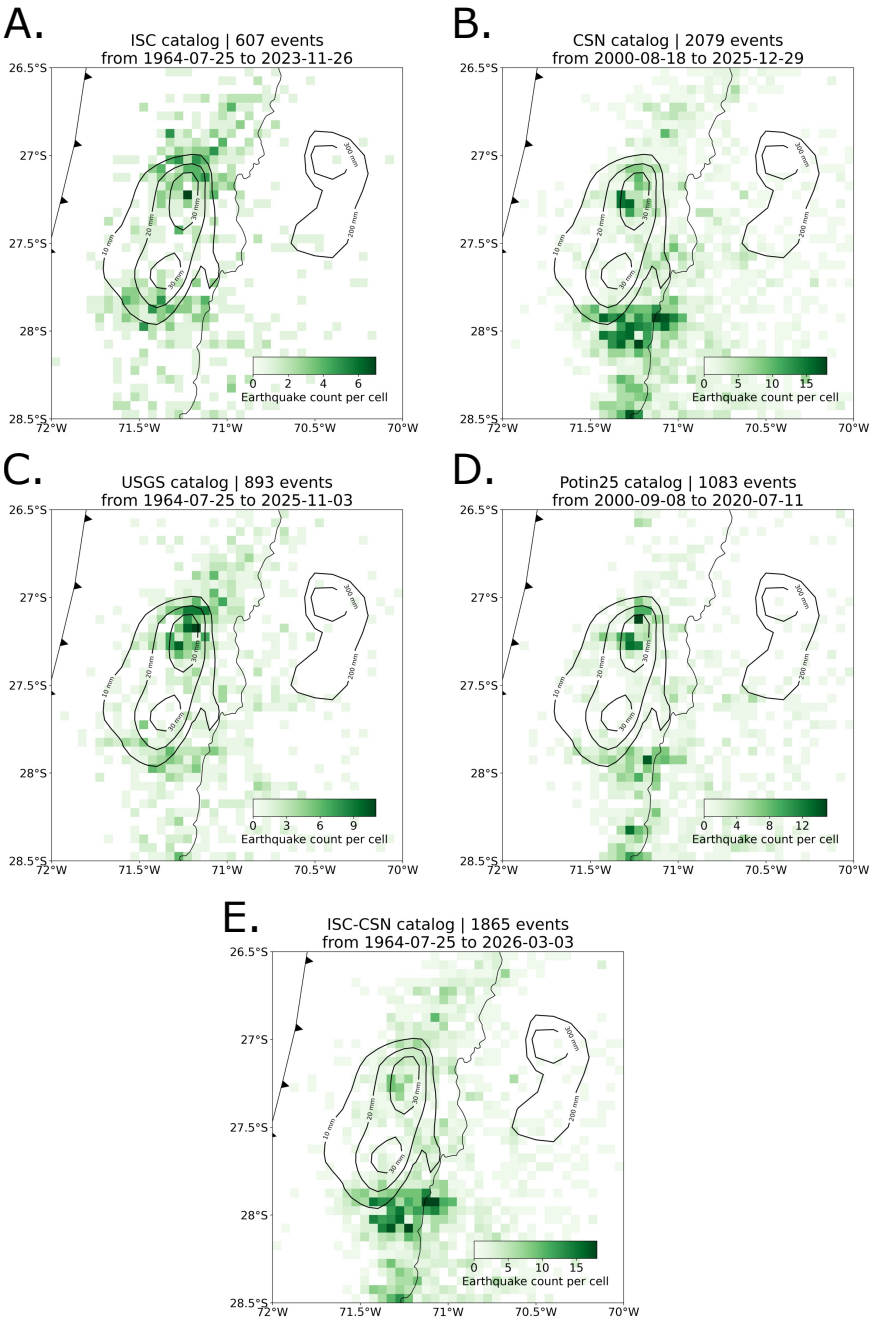

Figure S10: **Earthquake density plot for 4 catalogs**: A. ISC: 1964 - 2023; B. CSN: 2000 - 2025; C. USGS: 1964 - 2025; D. Potin et al. (2025): 2000 - 2020; E. ISC-CSN merged catalogs (ISC:1964-2012; CSN: 2012-2026), which is represented on Fig. 8. All catalogs are restricted to ± 15 km distance to the (Slab2.0 geometry Hayes et al., 2018).

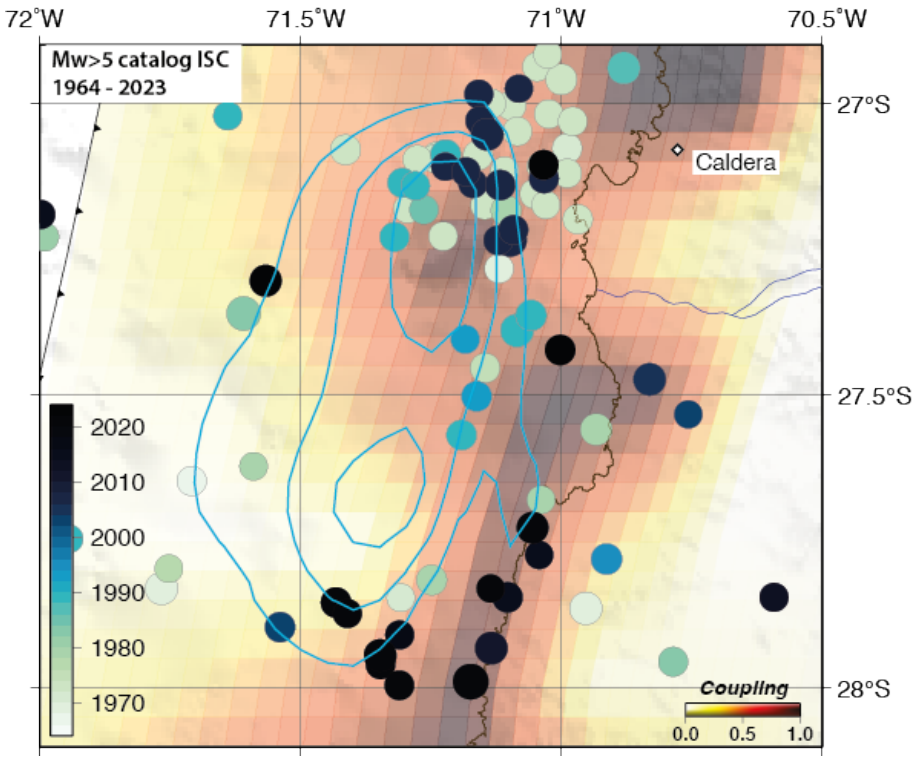

Figure S11: Earthquakes of Mw>5 since 1964 according to the ISC catalog in the region of interest, superimposed with the cumulative kinematic slip distribution obtained in this study and the coupling distribution from (Klein et al., 2018)

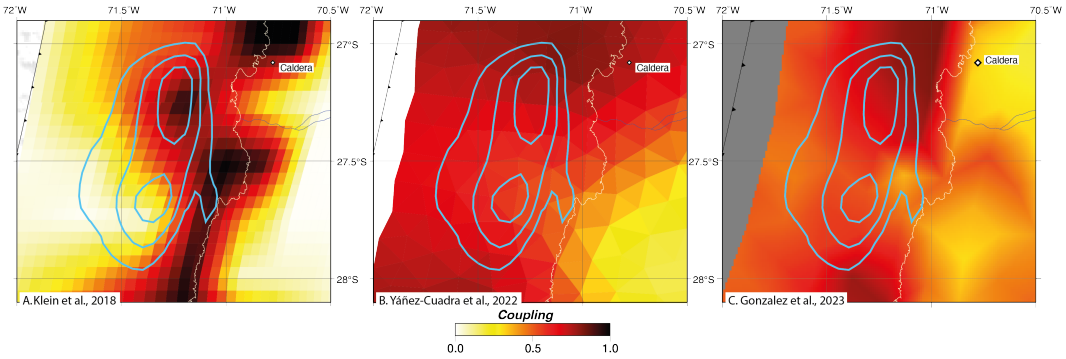

Figure S12: Comparison of the 2023 SSE cumulative slip distribution (blue contours) with the different coupling models in the region of interest, from left to right: Klein et al. (2018); Yáñez-Cuadra et al. (2022) and González-Vidal et al. (2023), all three coupling distributions are plotted with the same color scale.